Master of Science Thesis

CHARACTERISING DELAMINATION GROWTH IN COMPOSITES UNDER DYNAMIC LOADING USING INFRARED THERMOGRAPHY

An experimental approach to use an infrared camera to monitor delamination growth in composite test samples

Jagadeesh Narayana Swamy

Faculty of Aerospace Engineering · Delft University of Technology

TU Delft Delft University of Technology

CHARACTERISING DELAMINATION GROWTH IN COMPOSITES UNDER DYNAMIC LOADING USING INFRARED THERMOGRAPHY

An experimental approach to use an infrared camera to monitor delamination growth in composite test samples

Master of Science Thesis

For obtaining the degree of Master of Science in Aerospace Engineering
at Delft University of Technology

Jagadeesh Narayana Swamy

March 22, 2017

Faculty of Aerospace Engineering · Delft University of Technology

The authors acknowledge WMC Knowledge Centre, IRPWIND and SLOWind projects for motivating and partly funding the research.

Delft University of Technology
Faculty of Aerospace Engineering
Department of Aerospace Structures and Materials

GRADUATION COMMITTEE

Dated: March 22, 2017

Chair holder:

Dr. R. M. Groves

Committee members:

Dr. R. M. Groves

Dr. A. G. Anisimov

Dr. F. Lahuerta

Dr. S. J. Garcia Espallargas

Abstract

With an ever increasing demand for energy, the renewable energy sector is gaining a lot of importance. Among the various renewable energy sources, wind energy is becoming more attractive compared to its counterparts (solar, biomass, etc.). Some of the main advantages of wind energy are faster payback time and that power generation is possible both during the day and night. The wind energy industry is constantly aiming at larger size rotors for increased power generation and these larger rotor blades demand stronger and more durable materials. Currently, composite materials are extensively used for wind turbine blades. With a large heterogeneity in composite materials and complications in manufacturing processes, defects in composites are inevitable. A variety of defects and damages can be seen in wind turbine blades. Composites with such defects and damage undergo a significant loss in their mechanical properties. For the use of composites as a structural material, a good knowledge of possible defects and their behaviour should be understood. To do so, the behaviour of defects under different load conditions should be assessed. Many techniques such as ultrasound scans, X-ray radiography, etc. are available to detect the defects in composites, whereas studying the damage growth in a composite is still a challenging process.

In this research, a method has been developed to use thermography for characterising the delamination under dynamic loading. To demonstrate this method, a test sample with double shear configuration (DSC) and an initial delamination consisting of a Polytetrafluoroethylene (PTFE) insert was developed. The test sample was tested under fatigue loading and an infrared (IR) camera was used to monitor its thermal response and the delamination growth during loading. The data from the thermal camera was processed in two steps, firstly, fast Fourier transform (FFT) was used to transform the raw data from time domain to frequency domain. In the second step, FFT thermographs were further processed using an image segmentation algorithm. Here, the thermal plots are segmented to separate the delaminated and un-delaminated areas. By computing the number of pixels in the delaminated region, the area of delamination was obtained at each cycle and was plotted against the cycles to failure. The strain energy was computed with the help of force and displacement data from the test machine. Such signals allowed computing of the fatigue propagation curves and an understanding of the fatigue behaviour of the test samples.

The results from this research were promising as the delamination behaviour reported using this method was in good accordance with a reference visual inspection method. The quantifiable output from this method can be a good starting point to study delamination experimentally and computationally. In future, this technique could be extended to different test types that cannot

be quantitatively analysed using the conventional testing methods. The research was also presented at the European Conference on Composite Materials ECCM17, Munich, Germany.

"Learn some things from those who know;
Watch some things from those who do;
Learn the rest by self experience."

— **Sarvajna*

It is known that we cannot learn everything in this world, all by ourselves. The way to learn is by listening to those who know, others by watching those who do and the rest by doing it ourselves.

*Sarvajna (Sanskrit meaning "all-knowing") was a poet, moralist, philosopher and saint who is conjectured to have lived in the late 16th century (1570) in India.

Acknowledgment

During my last two years of stay in the Netherlands, there are a lot of people who directly or indirectly helped me in many aspects. So I think this is the right occasion to express my sincere gratitude to all.

Firstly, I thank TU Delft for giving me a wonderful opportunity to do my master's studies and WMC Knowledge Centre for welcoming me to do my research work.

At WMC Knowledge Centre, I thank F. Lahuerta and R. Nijssen for supervising and providing me the essential feedback's throughout my research. I also extend my gratitude to Koen for helping me with manufacturing at the laminate room, Sandra for facilitating all the administrative works and Sibrand, Martijan and others who carpooled with me, without whom it was impossible to reach office.

At TU Delft, I thank A. Anisimov and R. M. Groves for supervising my thesis along with providing valuable suggestions which turned out be very important in the successful completion of my thesis. I also thank all the lecturers and fellow students who played an important role in the completion of my master's degree.

Finally, I would like to thank my friends and family. I thank all my friends who helped me find a home away from home and I wish them a very successful career. I also extend my greatest love and gratitude to my mum and dad. Special thanks to my aunt Sujatha and cousin Balu for their constant support and good wishes.

Delft University of Technology — Jagadeesh Narayana Swamy
March 22, 2017

Table of Contents

Abstract vii

Acknowledgment xi

Nomenclature xix

1 Introduction 1

1.1 Outline . . . 3

2 Background study, research goals and methodology 5

2.1 State of the art . . . 9

2.2 Research question . . . 10

2.3 Approach . . . 11

3 Design and manufacturing of test samples 13

3.1 Material definition . . . 13

3.2 Design and manufacturing of test samples . . . 14

3.3 Defect definition . . . 16

3.4 Dimensions . . . 17

3.5 Fibre fraction . . . 19

4 Design of experimental setup and test plan 21

4.1 Test setup . . . 21

4.2 Static test . . . 24

4.3 Fatigue test . . . 27

5 Infrared image processing techniques **33**
5.1 Causes for deterioration of IR images . . . 33
5.1.1 Vignetting . . . 34
5.1.2 Fixed pattern noise . . . 34
5.1.3 Bad or dead pixel . . . 34
5.1.4 Noise from the surrounding . . . 34
5.2 Recording procedure . . . 34
5.3 Different processing techniques . . . 37
5.3.1 Thermal contrast . . . 37
5.3.2 Thermal signal reconstruction . . . 37
5.3.3 Principal component thermography . . . 38
5.3.4 Pulsed phased thermography . . . 38
5.4 Signal to noise ratio . . . 42
5.5 Image segmentation . . . 43
5.5.1 Segmentation by edge detection . . . 44
5.5.2 Segmentation by thresholding . . . 44
5.5.3 Segmentation by region . . . 44
5.5.4 Segmentation by clustering . . . 44

6 Test results and discussion **49**
6.1 Experimental results . . . 49
6.2 Processed thermal data . . . 50
6.3 Comparison of IR data with visible light camera data . . . 59

7 Conclusion and recommendations **61**
7.1 Conclusions from the research . . . 61
7.2 Recommendations for future research . . . 63

References **63**

References **65**

List of Figures

1.1 Size comparison between an Airbus A380 aircraft and a 154 m diameter wind turbine 2
1.2 Loads vs cycle graph of mega structures 3

2.1 Microscopic image of delamination damage between two plies (45° top and 90° bottom) 6
2.2 Scheme with (a) cyclic loading, (b) reversible process and (c) non-reversible process with hysteresis loop 8
2.3 Heating due to loss factor and thermoelasticity 9
2.4 Work flow of the research 11

3.1 Schematic representation of the resin infusion process 15
3.2 Steps involved in the manufacturing of test samples 17
3.3 Schematic representation of the test sample, all units are in mm 18
3.4 Actual test sample used for experiments 19

4.1 Image of the test setup used 22
4.2 Pictorial representation of the test setup, red lines represent power cables and green lines represent data cables 22
4.3 (a) FLIR 315 camera, (b) Block diagram and working of an IR camera 23
4.4 Loading conditions for static tests 25
4.5 Stress vs displacement graph of static tests 26
4.6 S-N curve of fatigue test performed 28
4.7 Image of the test samples before the test 29
4.8 Image of the test samples after the test 30

5.1 (a) CFRP laminate with 25 PTFE inserts as defect of different sizes and at different locations. (b) Raw image with vignetting and bad pixels. (c) Fixed pattern noise 35
5.2 The approach used for processing thermal images 36

5.3 Time and frequency response (a) Two temporal pulses of (i) 15 ms and (ii) 30 ms duration, (b) Corresponding frequency spectra . . . 39
5.4 Representation of single pixel in 2D . . . 40
5.5 Representation of several frames over time in 3D . . . 40
5.6 Temperature plot with colour map . . . 41
5.7 Amplitude plot with colour map . . . 41
5.8 Selection of locations for SNR calculation in temperature image . . . 42
5.9 Selection of locations for SNR calculation in processed image . . . 43
5.10 Representation of single pixel in 2D . . . 47

6.1 Type of failure during F_{max} and F_{min} loads. All units are in mm . . . 51
6.2 The flow chart of the research, consolidating all the sections . . . 52
6.3 A typical test data record sheet from the test machine . . . 53
6.4 Strain energy vs cycles . . . 54
6.5 Corrected strain energy vs cycles . . . 54
6.7 The tracking of delamination at various cycles, the green marking represents the crack front. The darker region is the undelaminated region and the lighter region is the delaminated region . . . 56
6.8 Delamination growth rate curves (Area vs cycles) . . . 57
6.9 Fatigue propagation plots, ΔG vs $\frac{dA}{dN}$ . . . 58
6.10 Corrected fatigue propagation plots, ΔG vs $\frac{dA}{dN}$ . . . 58
6.11 Comparison of measurement by the IR camera and visible light camera . . . 60

List of Tables

2.1 Overview of defects and failure modes 6

3.1 Fabric used 14
3.2 Resin system 14

4.1 Static test matrix 26
4.2 Statistics of static test 26
4.3 Fatigue test matrix, load ratio $[R] = 0.1$ 29

5.1 SNR values 43
5.2 Comparison of various image segmentation techniques 45

6.1 Comparison of area measured by the IR camera and visible light camera. The difference in percentage is calculated using $\frac{A_{IR}-A_v}{A_{IR}} * 100$ 59

Nomenclature

Greek Symbols

Symbol	Description
δ	Displacement
δ_{max}	Maximum displacement
ϵ_s	Axial strain
μ	Thermal diffusivity
σ	Stress
σ_{UTS}	Ultimate tensile stress
ϕ	Phase value
Φ	Loss factor

Others

Symbol	Description
$a_0, a_1..$	Coefficients of 1D Fourier solution
a	Crack length
A	Delamination area
$\bar{A}, \bar{B}$	Fatigue constants
$A_{c/s}$	Area of cross-section
A_{IR}	Area measured by an IR camera
Amp	Amplitude value
A_v	Area measured by the visible light camera
c, m	Curve fitting parameters
D	Lateral size of the specimen
da/dN	Crack growth rate
dA/dN	Delamination growth rate
dU_{max}/dN	Maximum strain energy release rate
f	Frequency
F	Force
F_{max}	Maximum force
F_{min}	Minimum force
F_n	Fourier function

$f(i,j)$	Input image for segmentation
$g(i,j)$	Output image after segmentation
G	Strain energy release rate
G_{max}	Maximum strain energy release rate
G_{min}	Minimum strain energy release rate
ΔG	Change in strain energy release rate
i,j,k	Local coordinates of a pixel
I	SVD matrix
Im	Imaginary part
k	Image index
K	Stress intensity factor
ΔK	Change in stress intensity factor
L	Diagonal matrix
$Max_{intensity}$	Maximum intensity of the object in the image
$Min_{intensity}$	Minimum intensity of the object in the image
$M \times N$	Rows $\times$ columns of a matrix
n	Image sequence
N	Number of cycles
N'	Total number of thermographic images
N_{max}	Maximum cycles to failure
N^0_{Color}	Colour map
n_x	Number of pixels in x-direction
n_y	Number of pixels in y-direction
n_z	Number of frames in z-direction
p	Degree of Fourier equation
Q^{heat}	Volumetric internal heat
R	Stress ratio
Re	Real part
t	Time
T	Temperature
$T(t)(i,j)$	Temperature evolution in 2D space
T_d	Temperature of defective region
$Thr, Thr0, Thr1$	Threshold values
T_s	Temperature of sound region
U_{max}	Maximum strain energy
$\bar{U}$	Orthogonal matrix
V_n	Noise strength
V_s	Signal strength
V^T	Transpose of orthogonal matrix
$W^{Loading}_{1-2}$	Mechanical strain energy in loading condition
$W^{Un-loading}_{2-1'}$	Mechanical strain energy in unloading condition
ΔW_{loss}	Loss in mechanical strain energy
Z	Depth of inspection

Acronyms

AE	Acoustic emission
CFRP	Carbon fibre reinforced polymer
CNC	Computer numeric control
COV	Coefficient of variance
DSC	Double shear configuration
FFT	Fast Fourier transforms
FLIR	Forward looking infrared
FPAs	Focal plane arrays
FPN	Fixed pattern noise
GFRP	Glass fibre reinforced polymer
IR	Infrared
IRT	Infrared thermography
NDT	Non-destructive testing
OCT	Optical coherence tomography
PCT	Principal component thermography
PPT	Pulsed phase thermography
PTFE	Polytetrafluoroethylene
SERR	Strain energy release rate
SIF	Stress intensity factor
S-N	Stress against the number of cycles
SNR	Signal to noise ratio
SVD	Singular value decomposition
TSR	Thermographic signal reconstruction
VOx	Vanadium oxide
UD	Uni-directional
USB	Universal serial bus

Chapter 1

Introduction

The use of composite materials has tremendously increased in the last couple of decades and they have started replacing metals in several major applications. The prime reasons for composites being attractive materials for industrial giants are high specific strengths and stiffness, superior fatigue properties and the ability to provide a unique benefit of tailoring the material properties according to the need [1]. The major consumers of composite materials are aerospace and wind energy industry. Since the cost of jet fuel and the demand for renewable energy are at their peak, composite materials are one of the prime alternatives at present.

Earlier, the use of composite materials in the aerospace industry was restricted to secondary structures alone, contributing to a maximum of 2% of the total weight of the entire aircraft [2]. In recent times, with increasing knowledge about these superior materials, their use has been increased to more than 50% of the total weight of modern aircraft [2]. The best examples for this are the Boeing 787 and Airbus A350. Likewise, the wind energy industry is also growing rapidly and started producing large rotor blades of lengths 60 m to 80 m [3]. Figure 1.1 gives an overview of the size comparison between the Airbus A380 aircraft and a 154 m diameter wind turbine. With such a fast growth, it is predicted that the wind energy industry will take over the aerospace industry as the leading user of composites and will account for nearly 60% of the market by the year 2020 [3].

With so much of advancement in the field of composites and their application, researchers have been constantly working on understanding the different aspects of composite materials like manufacturing, design optimisation and damage mechanisms. A lot of attention is directed towards understanding the behaviour of composite structures under different loads and damage mechanisms. Once the damage mechanism is understood and predicted accurately, further optimisation in the design of composites is possible that would lead to an increase and efficient use of composite materials.

Figure 1.2 clearly explains how different mega structures are loaded. For example, commercial aircraft experience heavy loads compared to wind turbine blades but the duration or the number of cycles are 3 orders less than wind turbines. Wind turbine blades are designed for low loads and high cycles (10^9 cycles or more) as they are expected to operate for 20-30 years [5].

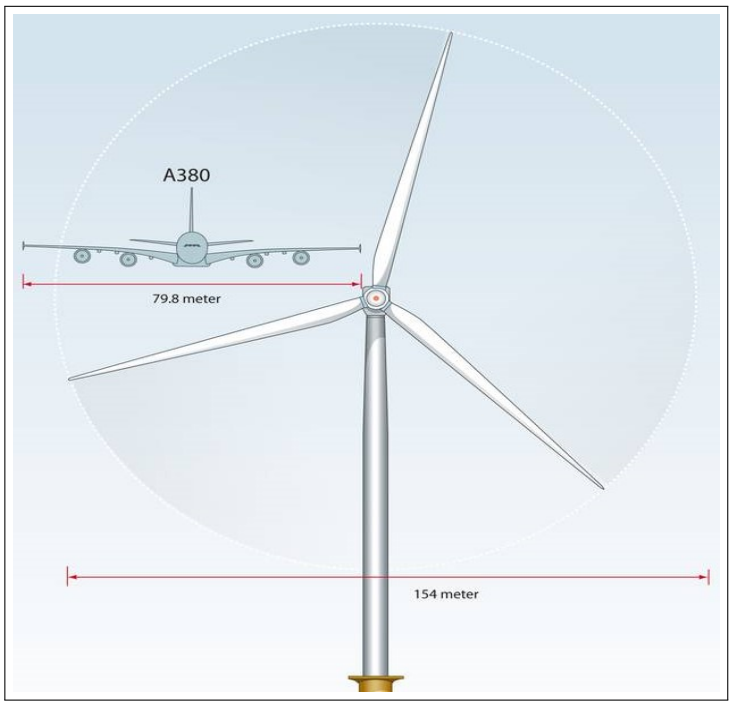

Figure 1.1: Size comparison between an Airbus A380 aircraft and a 154 m diameter wind turbine [4]

The common failure modes under fatigue loading are fibre cracking, matrix cracking and delamination [6]. In practice, different mechanisms contribute to material degradation at different stress levels. At high loads, it is fibre failure which is more dominant but high loads seldom occur, maybe once in 10^3 or 10^4 cycles [6]. Whereas, the medium and low loads that are experienced often are mostly responsible for matrix cracking and delamination failure modes [6].

Delamination is considered to be a serious problem and has drawn considerable attention from various research groups working on composite materials [7–10]. As delamination occurs within the laminate, it stays inside the laminate showing no abnormality on the surface of the structure. It is not easy to detect the delamination with the conventional inspection methods. However, the presence of delamination can hugely decrease the mechanical properties of the composite structure. Moreover, delamination has a tendency to grow faster under the influence of fatigue loading and if left unnoticed, it would lead to a catastrophic failure of the structure.

Fatigue testing is one of the technique that can characterise the material. For a greater knowledge on the fatigue behaviour and damage characterisation, in-situ characterisation techniques are necessary. There are several non-destructive testing methods, among which only the acoustic emission (AE) technique is used as an in-situ damage characterisation technique due to the fact that it identifies failure events as they occur [11].

In recent times, the testing technique that has been widely studied for material testing is thermography. The main advantages of thermography are: 1) contact-less inspection, which makes it a useful tool to inspect unreachable parts, 2) a larger surface area (up to few m^2) can

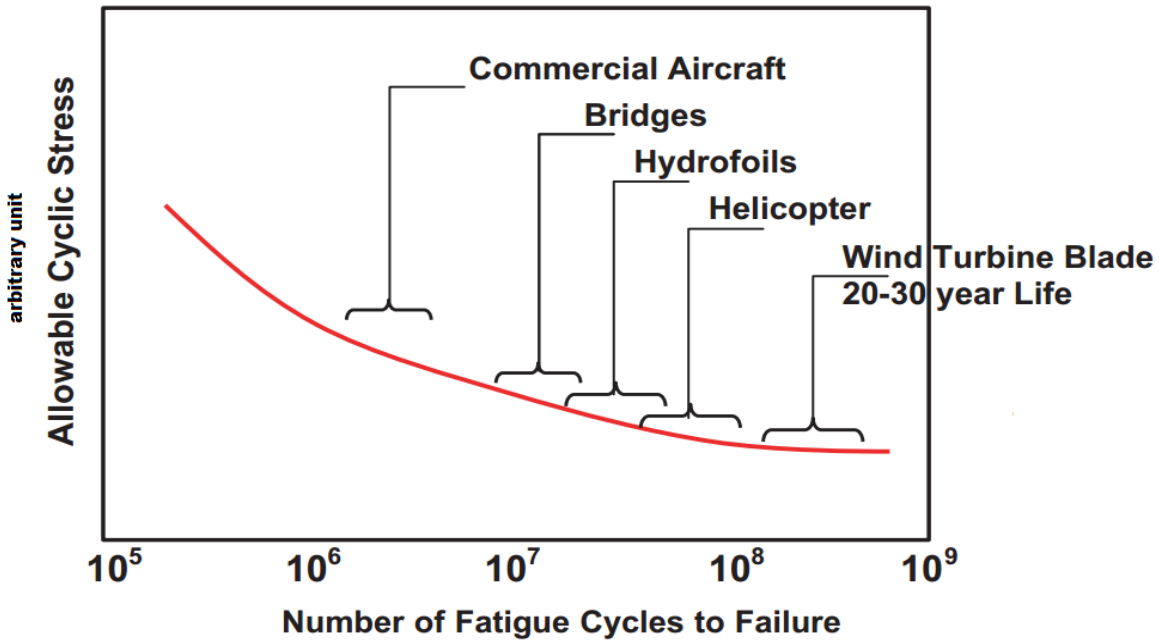

Figure 1.2: Loads vs cycle graph of mega structures [5]

be scanned, which quickens the process, 3) inspection can be performed both on flat surfaces and partially curved surfaces, however, partially curved surface inspections are not as easy as flat surface inspection, 4) inspection is also possible in the dark and it is better as it reduces the influence of reflection and unwanted signals, and 5) the infrared radiation involved during the inspection is not harmful, which makes the process safe for the inspector [12].

Most of the research in the past, related to thermography technique is restricted to static testing. The fatigue test studies involved in monitoring the change in the temperature when the material is loaded and correlating with the residual strength of the material [13, 14]. A few papers also contributed towards the inspection of composites using passive thermography and compared the results with benchmark inspection tools like ultrasound scanning [15, 16].

During the literature survey [17], it was clear that very few researchers have attempted to use IR thermography for quantitative analysis of the defect size. Clearly, no attempt has been made to use IR thermography for the quantitative analysis of composites under dynamic loading. So in this research, infrared thermography (IRT) has been used as a tool for the quantitative analysis of damage growth in composites under dynamic loading.

1.1 Outline

This section explains the structure of this document and it is planned as follows:

Chapter 2 presents the reader with a brief background information on the delamination failure modes that are seen in composite materials. This is followed by a review of the work of previous researchers in using IRT to characterise the defects in composites. Finally, the chapter finishes by defining research goals for this thesis based on the literature review.

Chapter 3 presents the materials used, design concept and manufacturing process used for the test sample preparation, in order to perform the research according to the question raised in Chapter 2.

Chapter 4 presents a detailed explanation of the test setup used for the experiments and also explains the equipments used for the test.

Chapter 5 presents a detailed explanation of the processing techniques used to process the thermographs obtained during the experiments performed in the previous chapter.

Chapter 6 presents the results of the experiments and a discussion is made on the results obtained.

Chapter 7 concludes the research by explaining the benefits and limitation of the thermography technique and recommendations are made for future research in this field.

Chapter 2

Background study, research goals and methodology

Chapter summary *Prior to this research, a literature survey was done in order to understand common defects and failure modes in composites and also to gain an insight into the state of the art. This chapter presents the reader with the background knowledge on delamination failure modes that are seen in composite materials. Thereafter, a short review is made of the work of previous research on the IRT for the characterisation of defects in composites. From this review, a gap in the literature was identified and the research goals of the current project were defined. Finally, this chapter finishes by describing the approach and methodology used to accomplish the defined research goals.*

By nature, composite materials are inhomogeneous with a large scatter in their material properties. Additionally, the complications encountered in the manufacturing process, makes composite materials more susceptible to defects. Some common defects seen in composite materials are voids, dry spots, fibre waviness and delaminations. A detailed explanation of defects was made as a part of the literature study [17]. Among all the damage modes in composites, delamination is considered to be the most menacing because it cannot be visualised externally without sophisticated techniques. Furthermore, it has a tendency to grow internally between the fibre layers under the influence of repetitive loads before failing catastrophically.

Delamination is defined as an area of poor or no bonding between adjacent layers in a composite laminate. Often, defects like voids, waviness and dry spots can also contribute to delamination under dynamic loads [18]. Figure 2.1 shows the delamination in a composite part and Table 2.1 indicates how other defects eventually transform into delamination. Hence, numerous experimental and computational techniques are required to characterise the delamination in composites and enhance the usability of composites as a structural material.

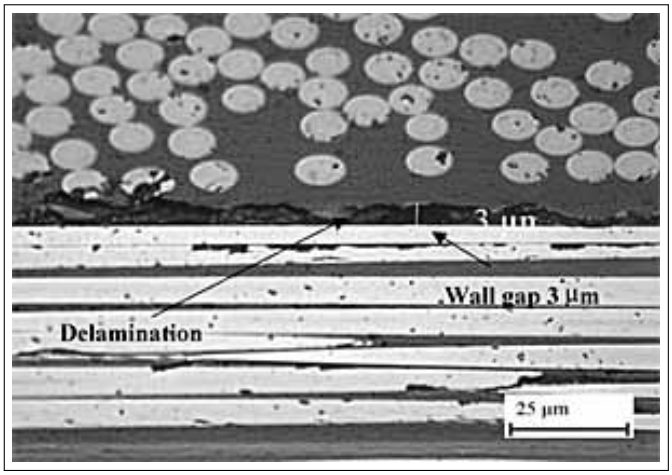

Figure 2.1: Microscopic image of delamination damage between two plies (45° top and 90° bottom) [19]

Table 2.1: Overview of defects and failure modes [17]

Defects	**Cause**	**Consequence**	**Common failure mode**
Voids	Leaks in the mould, fibre architecture & dissolved gases.	Matrix-dominated properties are affected & inter-laminar shear strengths are decreased, an increase in the moisture absorption is observed.	Matrix cracking & **delamination**
Fibre ply waviness	Large size fibres, lay up errors, skewed fabric & geometric changes.	Leads to delamination, matrix failure & reduced fatigue properties.	**Delamination**
Dry spot	Resin reaches outlet before complete infusion of the part.	Delamination & reduced mechanical properties.	**Delamination**
Surface defects	Poor quality of mould.	No effect on mechanical properties but aerodynamic properties are affected.	—
Delamination	Voids, contamination by foreign materials and poor resin infusion.	Mechanical properties are reduced.	**Delamination**

To predict delamination onset, growth and eventually the performance of a composite structure with the defect, some failure prediction methodologies have to be employed. In general, two approaches are widely used for this purpose, namely:

- Stress-strain approach
- Fracture mechanics approach

The stress-strain method is mainly focused on finding the fatigue life of a component or structure by developing S-N curves at different stress ratios (R) [20]. This method gives no information about the delamination or crack growth rate, it only considers maximum stress or stress amplitude for the fatigue life prediction [21]. The S-N curves are developed by conducting a series of tests with constant amplitude fatigue loads, at different load levels, and the cycles to failure are noted. The plot of maximum stress vs cycles to failure will give the S-N curves. In this way, the fatigue threshold limit can be identified for a given materials if it exists.

According to the fracture mechanics approach, failure in composites is associated with delamination growth [22]. Delamination occurs when the available strain energy exceeds the critical strain energy release rate of the material [22]. In this approach, the delamination growth rate da/dN is related to a fracture mechanics parameter such as strain energy release rate (SERR) or stress intensity factor (SIF). Generally, the fracture mechanics approach is based on the Paris relation. The Paris relation is given by Equation 2.1:

$$\frac{da}{dN} = c \cdot (\Delta K)^m \qquad \text{and} \qquad \frac{da}{dN} = c \cdot (\Delta G)^m \tag{2.1}$$

Where K is the SIF, a is the crack length, N is the cycle count, c and m are curve fitting parameters, G is the SERR and $\Delta G = G_{max} - G_{min}$.

In the case of multilayered composite structures, the SIF becomes a complicated parameter and SERR is a simpler parameter to characterise composites under fatigue loading. Further, during the process of unloading, G_{min} of the composite specimen rises artificially due to the facial interference resulting in the reduction of ΔG [23]. Therefore, it is challenging to obtain the correct value of ΔG. Meanwhile, the G_{max} value is easily available making it a desirable parameter to use [23].

Over the years, there is a high demand to develop a quantitative method to characterise the delamination in composites, to increase the fatigue reliability of composite structures [24,25]. Damage in composites is complicated as it involves multiple failure modes. Therefore, greater knowledge of the material and failure modes must be developed to understand the fatigue behaviour of composites. In the recent past, non-destructive testing (NDT) techniques had been extensively used to better understand the material behaviour compared to conventional techniques [13].

When composite samples are subjected to cyclic loads, a certain percentage of the mechanical strain energy gets converted into heat due to non-reversible processes; this is called as 'intrinsic dissipation' [26, 27]. The non-reversible transformation of the strain energy into heat is associated with material degradation, plasticity, damage and internal friction in the sample [28].

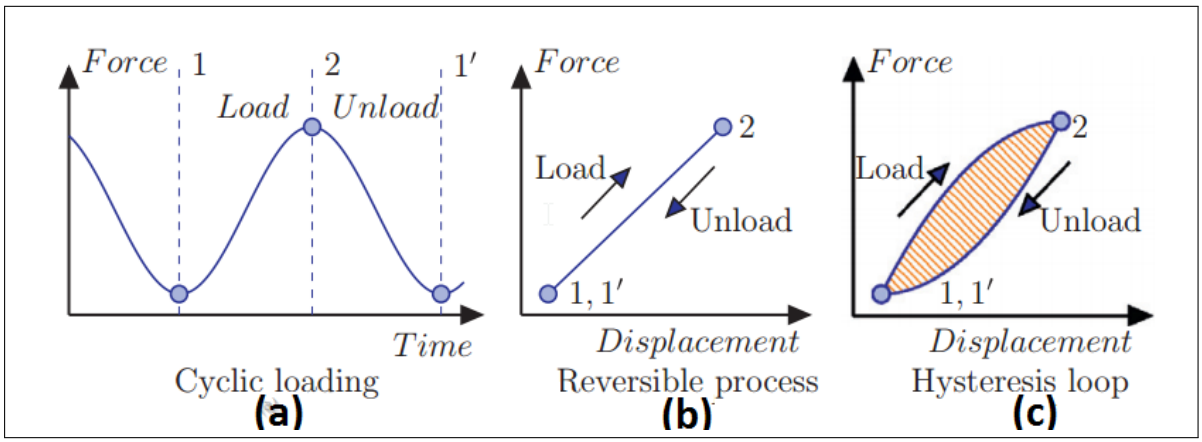

Figure 2.2: Scheme with (a) cyclic loading, (b) reversible process and (c) non-reversible process with hysteresis loop [28]

Figure 2.2a shows a typical cyclic loading with respect to time. In an ideal reversible mechanical process, the loading strain energy is equal to the unloading strain energy with no losses as in Figure 2.2b. But in the case of a non-reversible process, there is a certain degree of cycle hysteresis loss under sinusoidal cyclic loading and unloading as in Figure 2.2c [28].

In Figure 2.2c, a hysteresis loop is developed because the strain energy has built up when loading from points 1 to 2 i.e. $W_{1-2}^{loading}$ is different from 2 to 1′ i.e. $W_{2-1'}^{unloading}$ this loss in mechanical energy is defined by the equations below:

$$W_{1-2}^{loading} = \int_{1}^{2} \sigma \cdot d\epsilon_s \tag{2.2}$$

$$W_{2-1'}^{unloading} = \int_{2}^{1'} \sigma \cdot d\epsilon_s \tag{2.3}$$

$$\Delta W_{loss} = W_{1-2}^{loading} - W_{2-1'}^{unloading} \tag{2.4}$$

Where σ is the stress and ϵ_s is the strain. The loss of mechanical energy during a cycle is given by ΔW_{loss} which is related to the cyclic energy according to a loss factor. The loss factor (Φ) is defined as the ratio of energy lost to the elastic strain energy [28].

$$\Phi = \frac{\Delta W_{loss}}{W_{1-2}^{loading}} \tag{2.5}$$

The loss in mechanical energy is partially converted into internal heat. The volumetric internal heat flow (Q^{heat}) during cyclic loading can be expressed as [28].

$$Q^{heat} = f \cdot \Phi \cdot W_{1-2}^{loading} \tag{2.6}$$

Where f is the frequency of loading. In addition to internal heating, thermo-elasticity also contributes to a harmonic temperature variation depending on the thermal expansion coefficient. It can be seen from Figure 2.3, that a clear distinction between the heat due to thermoelasticity and internal heating due to hysteresis loss can be made.

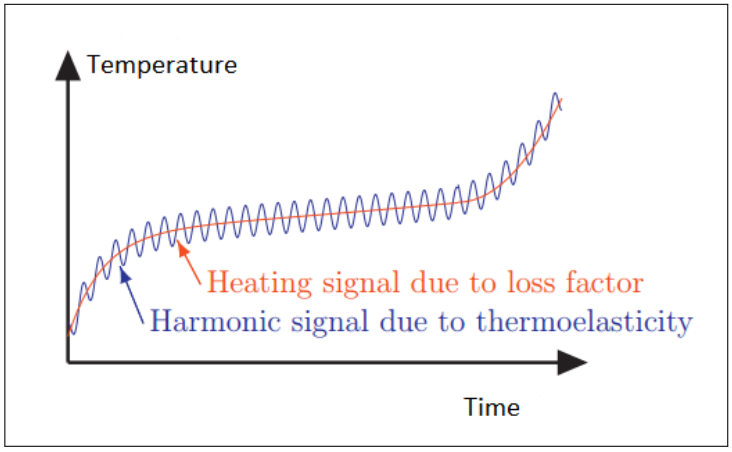

Figure 2.3: Heating due to loss factor and thermoelasticity [28]

From the above explanation, it is very clear that the material degradation or change in the material properties is always associated with the change in the temperature of the material. Hence, since IRT is based on the temperature change, it is the most suited technique to capture the change in the material temperature. Also, the comparison made with other techniques in the literature survey showed that the IRT has an advantage over its counterparts to monitor the fatigue behaviour of a composite sample [17]. Further, when compared to other techniques it is seen that IRT is more advantageous to monitor the fatigue behaviour. The main advantage of IRT is that it offers contactless inspection, large surfaces with areas upto a few m^2 can be scanned, it can be used in dark, the radiation involved during the inspection is not harmful and additionally this makes the process safe for the inspector. One sided inspection expands its usability as for most of the in-service objects, only one side is available for inspection. In the recent past, IR methods have been extensively used for in-situ inspections and monitoring. The digital output obtained from IR methods gives more clarity about the damage and defects in the material under inspection.

2.1 State of the art

A few references are available in the literature related to the use of IRT for damage analysis in composites. Colombo et al., (2014) [29] studied the influence of delamination on the mechanical behaviour of glass fibre composite. The study involved both static and fatigue tests of a glass fibre epoxy resin sample with a PTFE insert in the middle fibre layers to simulate delamination. The test results proved that the presence of delamination hardly has any influence on the mechanical properties in static loading. However, during the fatigue testing, it caused a significant reduction in the life of up to 40%. The thermal observations were made with an IR camera. The increase in temperature of the specimen as seen by the IR camera correlated with the accumulated damage. The authors of this paper also

proposed thermography as a tool for damage monitoring under both static and fatigue loading. The results of this experiment indicated that the change in material properties was always associated with the change in temperature, for the test speeds of 3 Hz - 5 Hz.

Lahuerta et al., (2015) [30] made a study of an open hole in a glass fibre sample, under fatigue in tension-tension loading with a thermal camera (FLIR 315) to record the tests. The test was conducted at 3 Hz. The thermal data was processed to get temperature plots which, on further processing using Fourier transforms and the amplitude plots of thermal signals measured by the IR camera, gave more insight about the accumulated damage. The final failure of the sample occurred in the same fashion as predicted from the amplitude plot.

Tighe et al., (2016) [31] performed a study on single lap joint samples to compare the detection performance for different type of defects using IR detectors and the pulse phased thermography technique (PPT). The defects were simulated using PTFE and silicon grease contamination. PPT clearly identified PTFE defects but not the silicon grease. When a small load was applied, a silicon grease defect was identified. This is claimed to be a portable and financially viable means of inspection for industrial application. Hidalgo-Gato et al., (2013) [32] compared several processing techniques and proposed that PPT and Principal Component Thermography (PCT) methods are suitable for processing IR images.

In conclusion, it is found that PTFE insert is the most commonly used material to simulate delamination in composite samples. Furthermore, it is found that though IRT is used extensively for damage inspection in composites, it is mostly restricted to qualitative damage analysis. However, few attempts have been made to use thermography for quantitative analysis of damage [30] [31] and this field of study is not fully explored.

2.2 Research question

Based on the literature survey, it was clear that very few researchers have attempted to use IR thermography for quantitative defect sizing and clearly, no attempt has been made to use IR thermography for quantitative analysis of composites under dynamic loading. By observing this gap in the literature, the research question is posed as,

"Can infrared thermography be a tool for quantitative analysis of damage in composites under dynamic loading ?"

Here, quantitative analysis refers to progressive damage monitoring in composites under dynamic loading. For example, if the damage is delamination, progressively tracking and computing the size of the delamination at each cycle is considered as a quantitative measurement. Once the delamination growth curves are computed, the fatigue properties can be easily obtained by calculations. These quantitative results from the thermography experiment could form a good basis for the development of damage mechanism models.

This gap in the literature seems to be an interesting starting point for a master thesis topic. To answer the preliminary research question, the sub-questions raised were:

1. *What kind of test samples and experimental setup should be designed to answer the main question?*
2. *Which thermographic processing techniques can be used to evaluate damage growth?*

2.3 Approach

The master thesis is divided into 3 major sections viz. the formulation of the research question, the experimental section and the processing section. The details are shown in Figure 2.4.

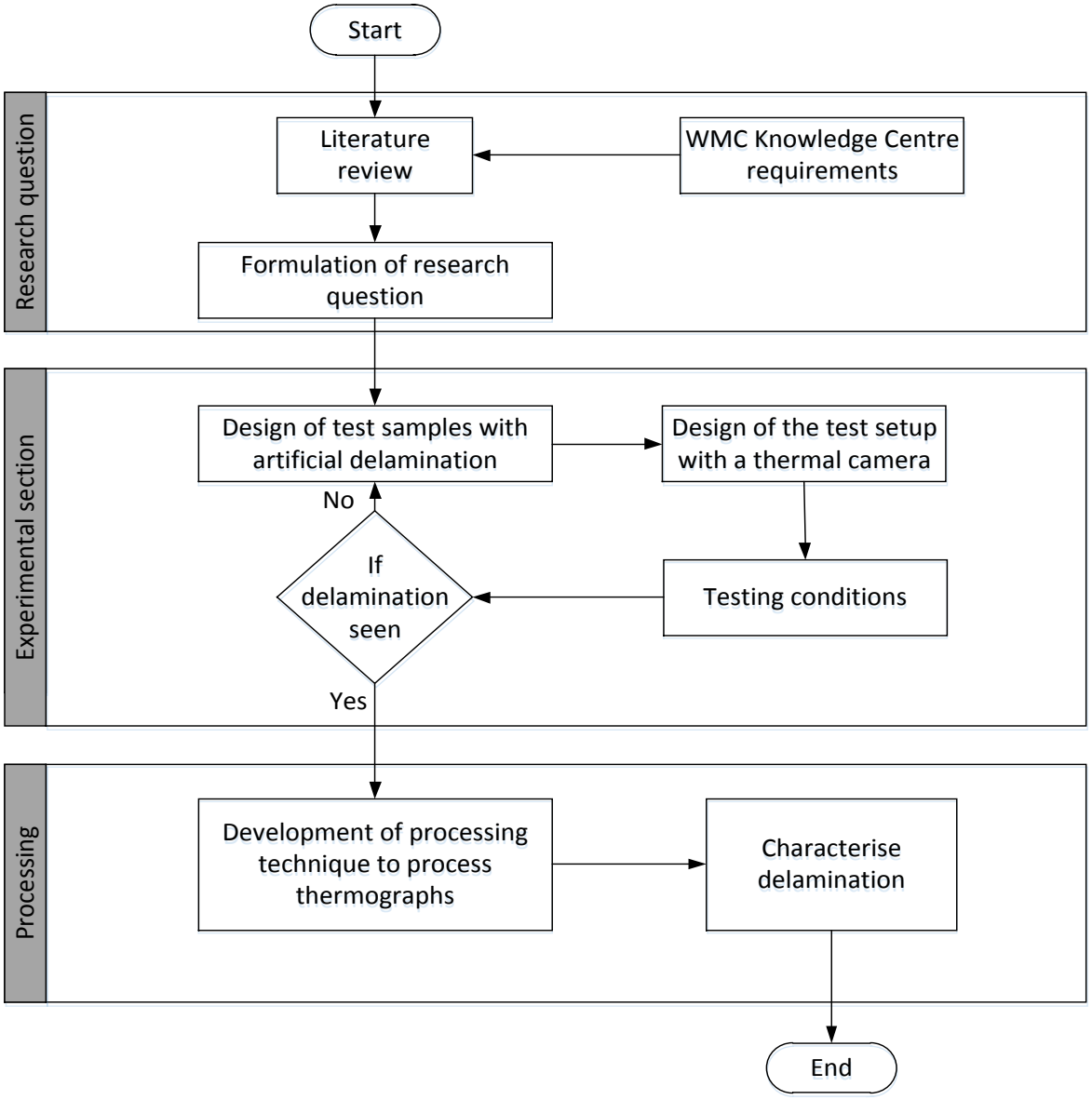

Figure 2.4: Work flow of the research

The research question is already formulated in the above section based on relevant literature while considering the requirements from WMC Knowledge Centre. The experimental section consists of 3 parts, namely, the design of the test samples with artificially simulated delamination, the design of the test setup with a thermal camera and the design of the test condition i.e. selection of stress ratio (R) and test frequency (f). The processing section consists of developing the processing technique to process the thermal recordings that are captured during the experiments. This processing technique should provide a comprehensive

understanding of the delamination behaviour. The detailed explanation of each section is presented in subsequent chapters.

This chapter comes to a conclusion with the research question and a brief discussion on the approach used for this research. In the next chapters, more about the design of test samples and test setup are explained.

Chapter 3

Design and manufacturing of test samples

Chapter summary *This chapter describes the materials used, design concept and the manufacturing method used for the test sample preparation. The main challenge was to design a test sample with artificial delamination. Simulating artificial delamination was not so straightforward as there was no standard method or technique to simulate delamination artificially in the test sample. Once the delamination design was finalised, the test samples were manufactured using the vacuum infusion method as it is the most widely employed manufacturing technique in the wind energy industry.*

After the research question was formulated in Chapter 2. The next step involved material selection for the experiments to conceptualise the design of the test sample, fabrication of the test samples, and the design of a test setup to capture the fatigue behaviour of the designed sample.

3.1 Material definition

The materials selected for the experimental part of this research was a wind turbine dedicated material i.e. the glass fibre reinforced polymer (GFRP) with glass fibre as a reinforcement material and their material properties are seen in Table 3.1. The matrix material is a two component epoxy with Epikote MGS RIMR 135 as resin and Epikur MGS RIMH 137 as curing agent, their material properties are seen in Table 3.2. These materials were selected for experiments as they are the standard materials used for all the research work at WMC Knowledge Centre.

Table 3.1: Fabric used [33]

Fabric	Article	Manufacturer	Areal weight $[g/m^2]$	Density $[kg/dm^3]$
Glass UD	S15EU910-00950-00600-100000	Sartex	948	2.6

Table 3.2: Resin system [34]

Components	Article	Manufacturer	Density $[g/cm^2]$
Resin	Epikote - Resin MGS BPR 135 G3	Hexion	1.13 - 1.17
Hardener	Epikure - Curing agent MGS BPH 137G	Hexion	0.93 - 1.00

3.2 Design and manufacturing of test samples

The commonly seen manufacturing processes in the wind energy industry are hand lay-up, resin infusion and prepreg lay-up processes. Hand lay-up is an inexpensive process but the quality yield of the final product is low. On the other hand, prepreg lay-up gives a high-quality product but it is an expensive process. Whereas, the resin infusion process strikes the right balance between the manufacturing cost and quality [17]. In the last decade, the infusion process was widely used by manufacturers around the world [17]. So, it was decided to use the resin infusion process to manufacture all the test samples for this research.

The resin infusion technique shall be briefly described; the dry fibres are placed in a mould without pre-wetting or saturating the fibres. A porous release film or peel ply is laid over the reinforcement and an infusion mesh is laid over that. The whole laminate is then sealed with the help of a vacuum bag and a sealing tape [35]. Resin inlet and vacuum outlet ports are created to facilitate resin entry, the placement of which, varies according to size and shape of the laminate. A schematic representation of the resin infusion technique can be seen in Figure 3.1.

Before manufacturing the test samples, it is important to decide the material, layup, the number of layers of fibres, the location and the size of the defect. Since the material has already been selected in Section 3.1, the next step is to decide on the lay-up and number of layers of fibre. For this research, the layup of the sample is chosen to be uni-directional (UD, 0° i.e. the fibres are placed along the loading direction) and PTFE (Teflon) material is selected to simulate artificial delamination in the composite sample as seen in many research works [29,31]. PTFE tape is widely used to mimic a defect in composites because it is simple and easy to include a PTFE insert during fabrication. More about the geometry and location of the defect is explained in Section 3.3. UD is chosen because it is a simple configuration and two failure modes are expected, one is delamination failure due to the presence of PTFE as an artificial delamination and the second one is fibre failure mode as UD fibres attract maximum load into them and they fail. The idea is to have a relatively thin section because

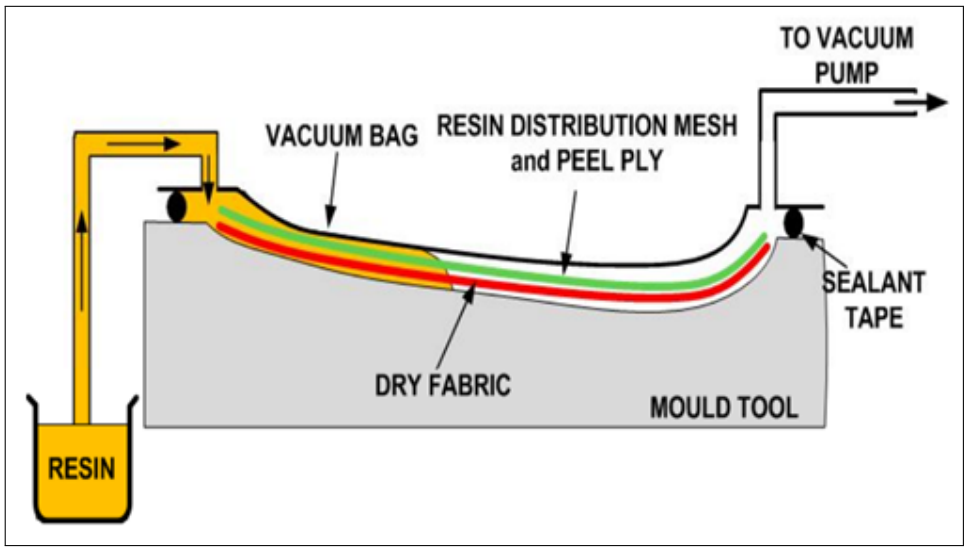

Figure 3.1: Schematic representation of the resin infusion process [35]

monitoring thin sections is more suitable for an IR camera [36]. Four layers of fibres were chosen, as four layers are relatively thin.

For the preparation of test samples, firstly the composite panel should be manufactured to the same configuration as discussed above. Once the panel is manufactured, the next step is to apply tabs to the panel. Tabs facilitate gripping of samples during the tests and to an extent avoid the failure of samples at the grips, as tabbing adds extra material making it stronger at the grips. After the application of tabs, the panel is cut into the standard test sample dimensions (ISO 527) [37].

The procedure employed for manufacturing the glass fibre and epoxy resin composite panel to the test sample of the required dimensions is explained step by step in this section.

1. An aluminium plate is used as a base mould for laminating. It is cleaned, prepared for the placement of fabric and taping the vacuum bag. Firstly, the plate is cleaned with ethanol then a scotch brite pad is used to scrape off any irregularities and recleaned with ethanol (see Figure 3.2a). Finally, a release agent is applied on the laminating surface to facilitate easy removal of the composite laminate from the mould surface.

2. The fabric plies are drawn from the roll (see Figure 3.2b) and the UD glass fibre plies are cut perpendicularly to the fibre direction (Figure 3.2c).

3. The cut plies are carefully transferred onto the aluminium plate and aligned.

    - At this point, the defect as PTFE is introduced into the fibre stacking (see Figure 3.2d). A detailed explanation of the defect is given in section 3.3.

4. Now tacky tape is applied around the perimeter of the cut fabric with a 2 cm - 5 cm gap.

5. The fabric placed is covered with peel ply (Figure 3.2e). The peel ply is overlaid with a release film and infusion mesh that helps in achieving an even distribution of the resin.

6. A runner is introduced and taped at the edge of the infusion mesh (Figure 3.2f) and the other end is connected to the resin bath via a tap.

7. The vacuum port is positioned away from the stacking and is connected to a vacuum pump through a connecting pipe that sucks out air from the bag.

8. Breather material is placed on top of the stacking and then, the bagging is finished by tacky taping all the sides while placing the vacuum bag on the top. Extra care is taken near the inlet and outlet of the pipes to avoid leaks.

9. The resin inlet tap is turned off and the pressure inside the vacuum bag is brought below 10 *mbar* with the help of a suction pump. This constant pressure is maintained for 20 *min* - 30 *min* to check for any leaks in the bag.

10. The pressure in the bag is slightly increased to around 150 *mbar*, i.e. a pressure greater than the resin degassing pressure.

11. The infusion process is started by turning on the inlet tap and waiting until the resin completely wets the fabric. Now the taps are turned off.

12. The infused laminate is left to cure overnight and the next day the de-bagging is done to get the panel out.

13. Once the panel is manufactured, it is cut into the required dimension by trimming off extra material. The tabs are applied at clamping ends of the panel and then the panel is cut precisely to get the test samples using a CNC machine.

3.3 Defect definition

Simulation of an artificial delamination as a defect was a complicated process. As the aim of the research was to capture delamination propagation, the test sample was designed in such a way that delamination is the predominant failure mode. To do this, a PTFE tape was used to introduce artificial delamination. The fibre cuts and PTFE were included in the laminate during fibre stacking. As shown in Figure 3.3, all four layers of fabric were cut at predefined locations. The 1^{st} and 4^{th} layers of the laminate were cut at location 1 and the 2^{nd} and 3^{rd} layers were cut at location 2. PTFE inserts were placed underneath the cut in the 1^{st} and 4^{th} layers i.e. location 1. As said earlier, the only reason to cut fibres was to make delamination a dominant failure mode by avoiding fibre from carrying all the loads and failing [38].

The above configuration for the test sample design was chosen because, when the load is applied, the 1^{st} and 4^{th} layers with PTFE inserts start to delaminate experiencing both mode 1 and mode 2 loads (peeling and shearing respectively). The matrix which is filled in the cut space of fabric in the 2^{nd} and 3^{rd} layers also starts to crack. But the damage growth on the external plies is predicted to be faster since they experience both mode 1 and mode 2 loading. The sample resembles the lap shear configuration on two sides and hence it is named as "double shear configuration" (DSC).

(a) Aluminium base plate during cleaning

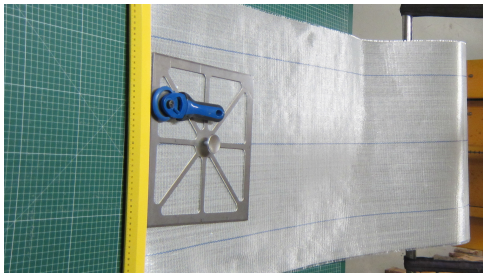

(b) Drawing of fabric from the roll

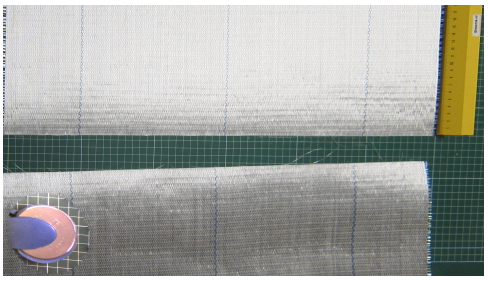

(c) Cutting of the marked fabric

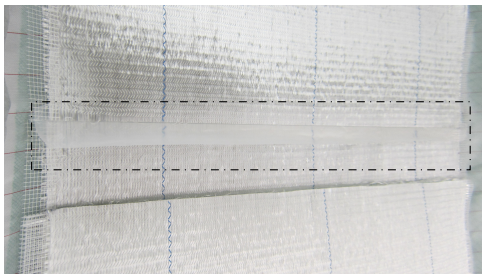

(d) Introduction of PTFE tape

(e) Spreading of peel ply over the stacking

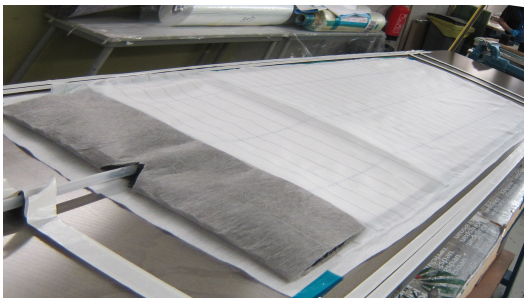

(f) Runner placed at the edge of infusion mesh

Figure 3.2: Steps involved in the manufacturing of test samples

3.4 Dimensions

The dimensions of the test sample were chosen according to ISO 527 standard for tensile testing [37]. ISO 527 gives the standard test procedure, dimensions of the sample and testing methods for evaluating the tensile properties of unidirectional fibre reinforced composite. According to this document, the gauge length of the sample should be 150 mm, the width 15 mm, the nominal thickness 3 mm (for four layers of fibre) and overall length with tabs is 250 mm. This can be seen in Figure 3.3.

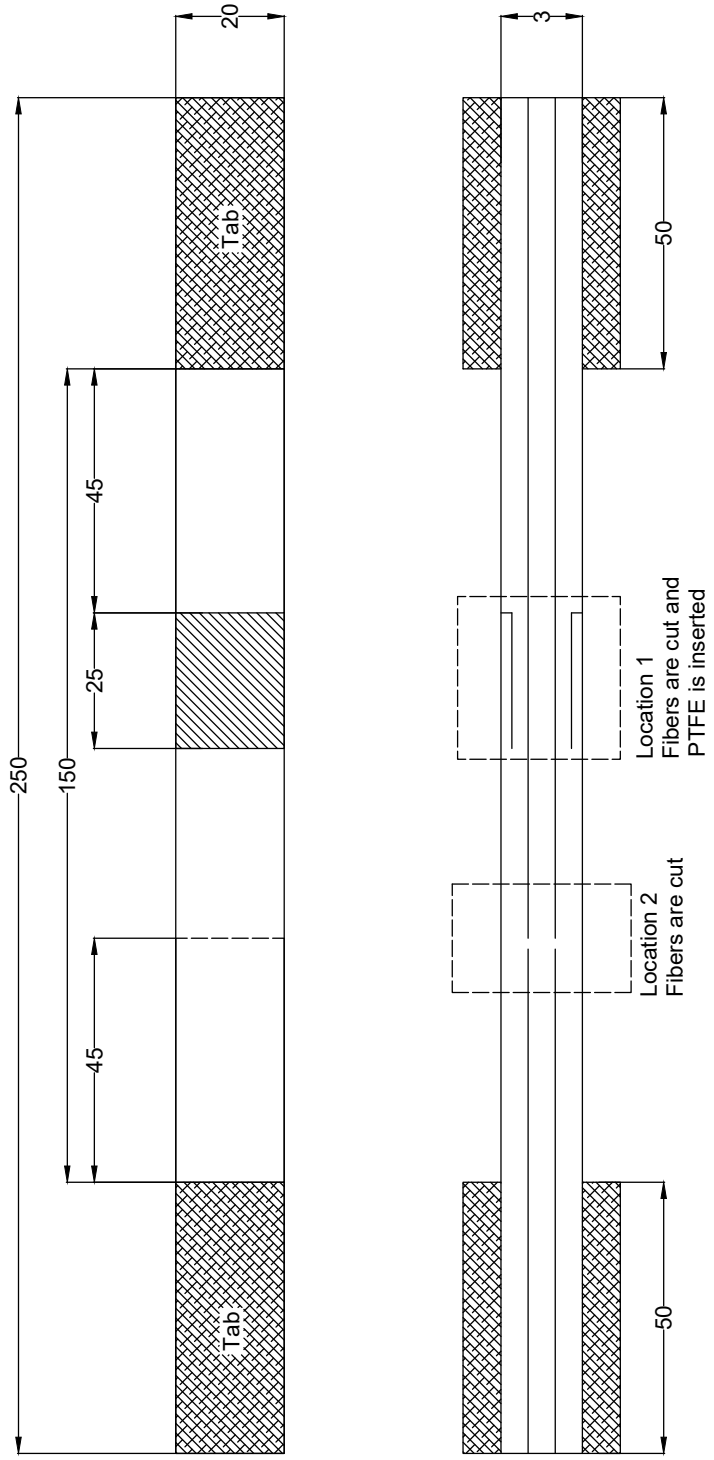

Figure 3.3: Schematic representation of the test sample, all units are in mm

3.5 Fibre fraction

After manufacturing the composite laminate with the resin infusion technique, the fibre fraction evaluation was performed on the composite laminate to understand its quality. The test samples were cut out of the laminate and the samples were named for easy identification. The ASTM D 2584 - 11 [39], standard test method was used to determine the fibre and void content of the laminate at three locations. The average fibre content and void content of the test samples were 62.35% of weight and 0.26% respectively. As the void content is less, it is a good set of test samples to proceed with the experiments. Figure 3.4 is an actual image of the test samples used for the experiment.

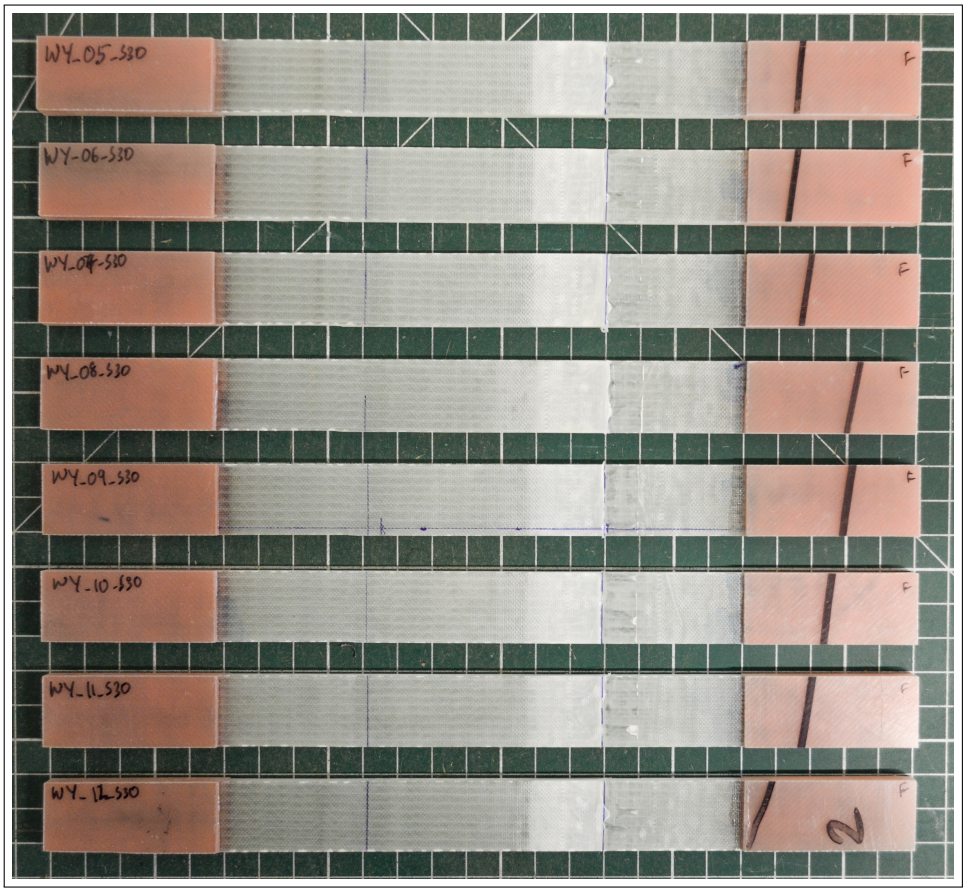

Figure 3.4: Actual test sample used for experiments

To conclude this chapter, the design, fabrication and defect simulation in the test sample are explained here. In the next chapter, the design of test setup and the experimental procedures are explained.

Chapter 4

Design of experimental setup and test plan

Chapter summary *This chapter presents the reader with a detailed explanation of the test setup used for the experiments while explaining the equipment used for the test. The main aim of the experiment was to study the fatigue behaviour of composites. To study the fatigue behaviour, firstly, the static tests were performed and later based on the static test results, the fatigue tests were planned.*

4.1 Test setup

This section explains the test setup used for both static and fatigue tests. The test setup remains nearly identical for both the tests, as illustrated in Figure 4.1. To provide more details about the connections, a block diagram is shown in Figure 4.2. Now, beginning with the test sample and going in the clockwise direction as in Figure 4.2, the test samples were clamped into the grips of the 100 kN test machine. Test machine is a hydraulic machine that was controlled by the 'WMCs', an in-house controller software on a dedicated computer. The WMCs software is developed by WMC and it is used for all the testing and research experiments at WMC Knowledge Centre laboratory. An IR camera FLIR 315 was used to monitor the ongoing tests which is shown in Figure 4.3a. The FLIR camera uses a bolometer as a detector. A bolometer measures heat from the source by sensing the temperature induced variations in the electrical resistance of an IR-absorbing material. A Wheatstone bridge circuit measures the heat absorption by comparing the resistance of a piece of the material that absorbed IR light to the resistance of an equivalent piece of an identical material that was kept in the dark.

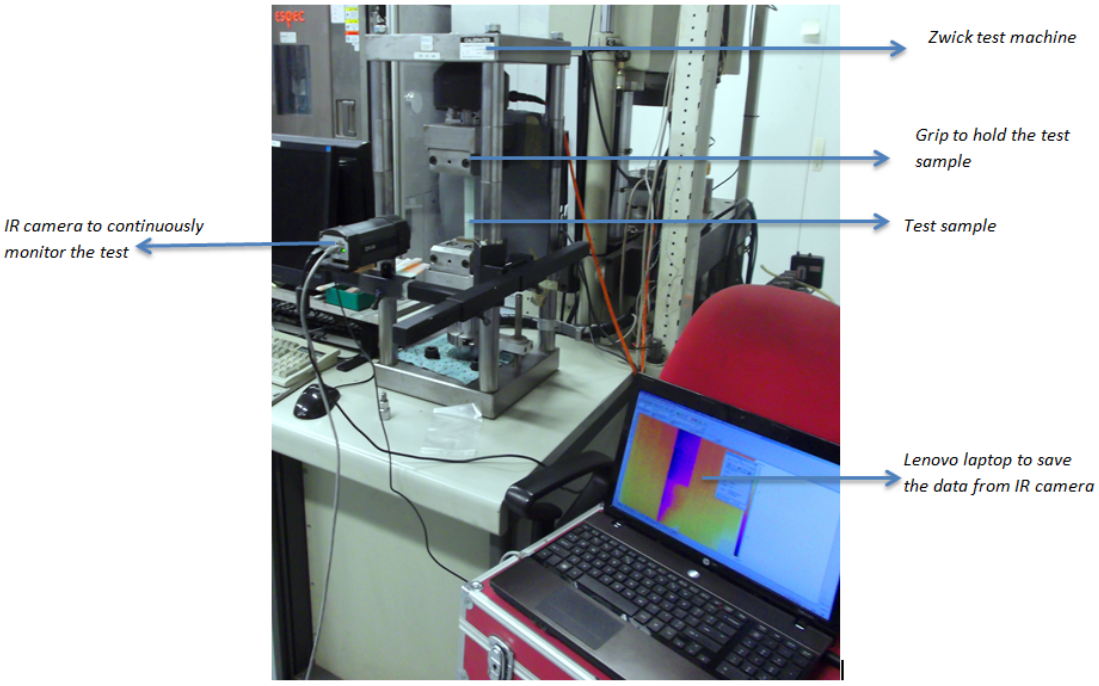

Figure 4.1: Image of the test setup used

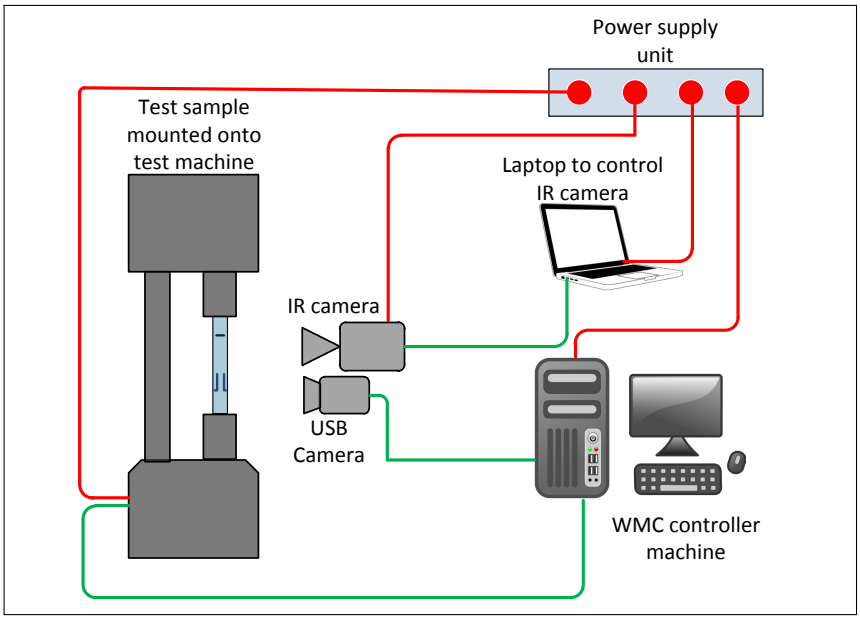

Figure 4.2: Pictorial representation of the test setup, red lines represent power cables and green lines represent data cables

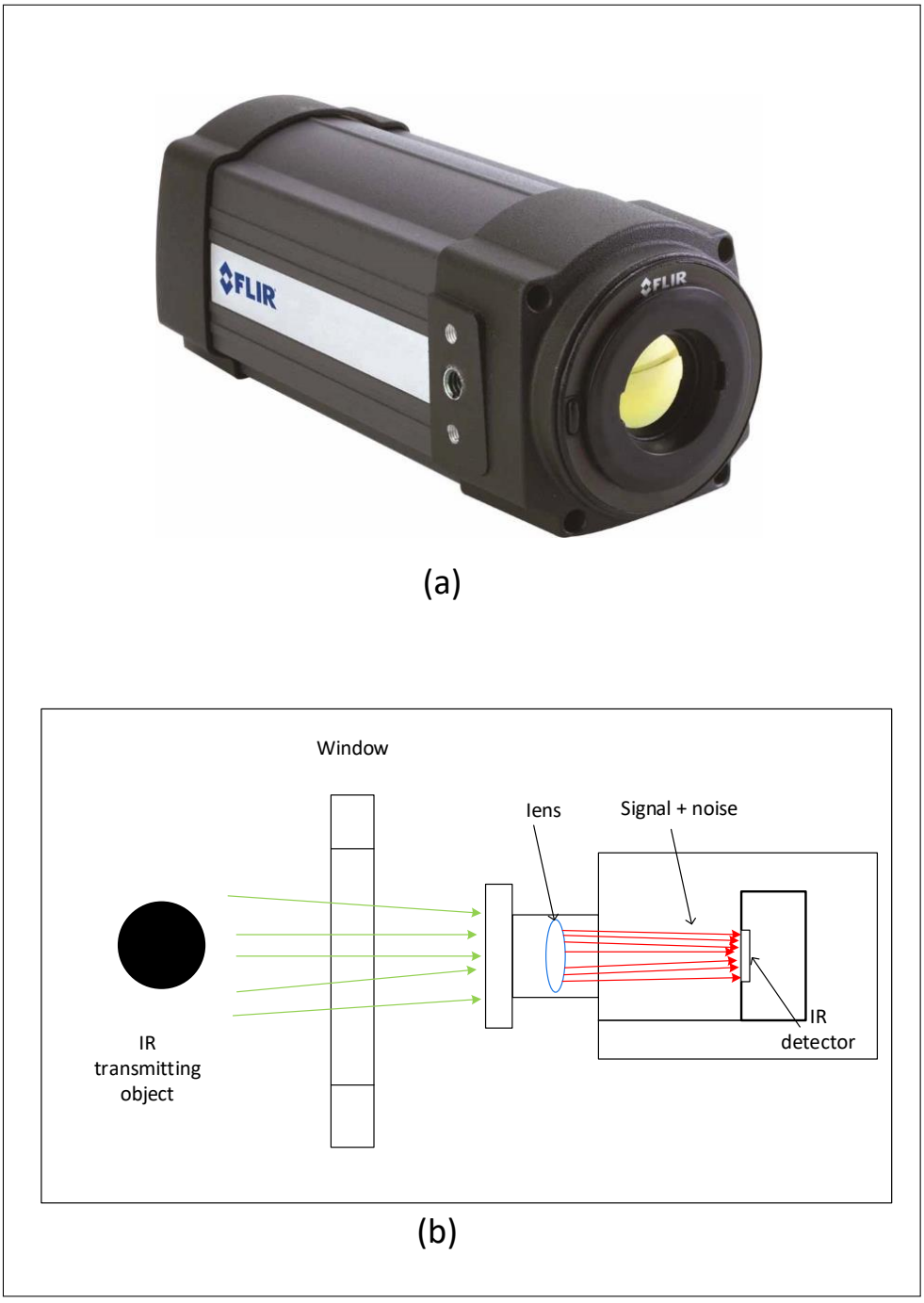

Figure 4.3: (a) FLIR 315 camera, (b) Block diagram and working of an IR camera

The IR systems majorly consist of five components, namely, the optical system, detector, amplifier, signal processing block and the display unit (mostly on the computer). The IR system can be schematically represented as in Figure 4.3b. The IR energy from the object was captured by the optical system; the received energy was then focused onto the detector with the help of a lens. Detectors are of two types: Thermal (for example, microbolometer) and Photonic (for example, a photoconductive detector).

A microbolometer measures the temperature variations caused by IR absorption in individual single pixels that are thermally separated and grouped into focal plane arrays (FPAs). There are majorly 2 types of IR absorbing materials used in microbolometers, namely Type 1 and Type 2. Type 1 is the pyroelectric or ferroelectric crystals which produce electrical signals that are directly proportional to the temperature increase caused by IR absorption. The most common material under Type 1 in use is barium-strontium titanate. Type 2 materials are thermistors, wherein the electrical resistance changes with temperature. The materials used in Type 2 category are semiconductors, amorphous silicon and vanadium oxide (VOx). The material used for FLIR 315 camera is VOx.

The IR camera was positioned right in front of the test sample with the help of a fixture. The IR camera was powered by the power supply unit and it was controlled by an FLIR software interface from a laptop. The tests were not recorded for the complete length, the reason for this is explained in detail in Section 5.2. To record the tests discretely, a small code snippet was used to switch the camera on and off according to the needs. A visible light USB camera was also mounted next to the IR camera to compare the delamination measured by it later. As it can be seen from Figure 4.2, the IR camera was controlled by a separate computer, not by the same controller that controls the test machine. So here, an issue is brought to the readers attention that there is a slight mismatch in the cycle count measured by the camera and the test machine. This was taken into consideration during post processing.

Apart from the above mentioned steps, extra care was taken to make the testing area free from disturbance, mainly to avoid the noise from the surroundings such as movement of men and/or machines. The test samples also had a rough surface finish on either side, this was achieved with the use of a peel ply during the manufacturing stage. Use of smooth or glossy surfaced sample was not suitable as these samples reflect different kinds of noise falling onto them and this causes more problems during processing.

4.2 Static test

First, the static tests were planned in order to characterise the material under tension. The tests were planned on 100 kN servo-hydraulic machines with 100 kN load cell. From previous material data at WMC database [40], the ultimate tensile strength of same grade UD glass fibre samples was 765 MPa with standard deviation and coefficient of variance being 18 MPa and 2.35% respectively for the sample size of 6. The cross-sectional area of the test sample prepared for the tests was $15 \times 3\ mm^2$ and according to Equation 4.1, the approximate maximum load requirement was 35 kN. Hence 100 kN machine was a good choice for the experiment.

$$F = \sigma_{UTS} \cdot A_{c/s} \tag{4.1}$$

Where, F is the force required to fail the sample in kN, σ_{UTS} is the ultimate tensile stress of the sample material in MPa and $A_{c/s}$ is the cross-sectional area of the sample in mm^2 i.e. width $\times$ thickness.

The steps followed for the static tests were as follows:

- The fabricated test sample was mounted onto the test frame. To do so, first, the bottom part of the test sample was clamped with slightly lower clamping pressure of 15-20 *bar* and a right angle alignment tool was used to get the sample parallel to the load. Once the alignment was completed, both the top and bottom clamps were closed with a hydraulic pressure of 120 *bar* - 150 *bar*.
- After mounting, the control parameters were fixed. The input load was zeroed so that the test could start from 0 kN.
- The test mode was chosen to be displacement control, the displacement channel was changed to zero and the loading rate was 2 mm/min. Figure 4.4 graphically represents the loading condition.

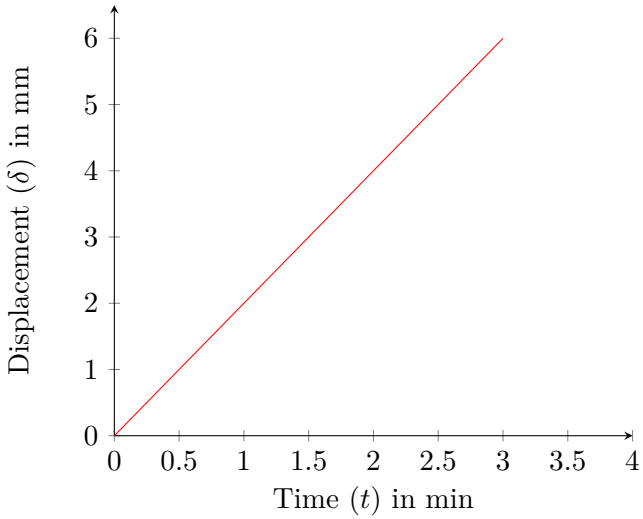

Figure 4.4: Loading conditions for static tests

- Once all the parameters were set, the tests were started and checked for the slip of the test sample. If there was no slip, the test continued till the failure. Once the test sample failed, the failure load and the displacement values were noted down. After all the test parameters were recorded, the test was brought to halt and this procedure was repeated for all the remaining samples.

The static tests were aimed at determining the maximum force. The force was measured through a load cell and the stress was known by the ratio of force to the area, expressed in MPa. Displacement was measured by the internal displacement of machine and strain can be calculated as a ratio of change in distances between the grips to initial distance between the grips. The tests were performed under displacement control and the ramp of the displacement is 2 mm/min as per ISO 570 standards.

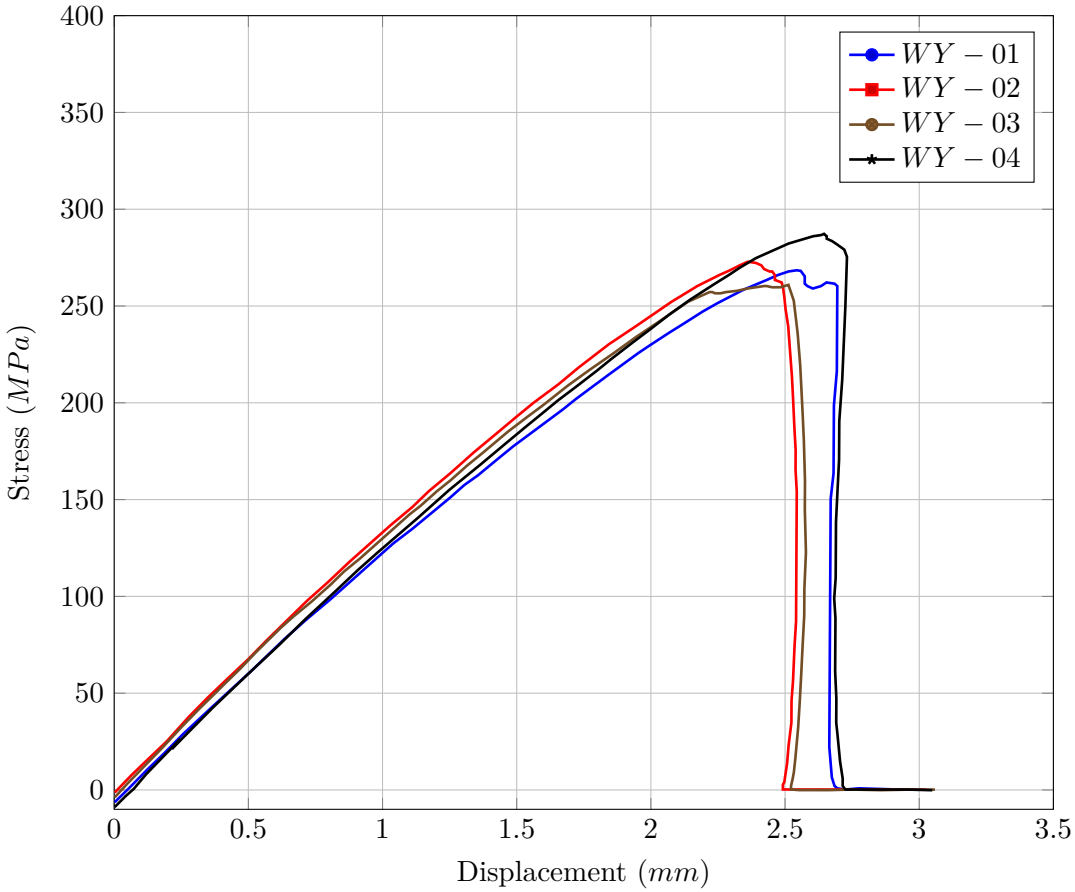

Figure 4.5: Stress vs displacement graph of static tests

Table 4.1: Static test matrix

Sample	**Width** $[mm]$	**Thickness** $[mm]$	**Length** $[mm]$	**Max. load** $[kN]$	σ_{UTS} $[MPa]$
WY-01	25.99	2.99	150.19	21.19	272.68
WY-02	25.5	3.24	150.08	21.5	260.22
WY-03	25.4	3.20	150.11	21.8	268.20
WY-04	24.99	3.00	150.02	21.4	287.63

Table 4.2: Statistics of static test

Sample count	**Average max. stress** $[MPa]$	**Coefficient of variance** $(\%)$	**Standard deviation** $[MPa]$
04	272.1825	0.04231	11.5157

Figure 4.5 shows the stress vs displacement graphs of static test and Table 4.1 shows the test matrix for static test. All the dimensions for length is in mm, force is in kN and stress is in MPa.

Table 4.2 illustrates the statistics of the static test results. According to the results, an

average maximum stress was found to be 272 MPa with the coefficient of variance (COV) of 0.0423 over four samples shows good repeatability of the test results. Further, the fatigue tests were planned based on the static test results.

4.3 Fatigue test

A number of fatigue tests were planned based on the maximum loads obtained from the static tests. For each fatigue test, the maximum load selected was a percentage of the static maximum load determined in the Section 4.2. The percentage depends on the minimum number of cycles that the sample was expected to undergo before failing. Usually, the load levels were selected to obtain a well defined S-N curve. In this case it is between 1000 cycles to 1 million cycles because there would be a lot of scattering below 1000 cycles and the test would be time consuming or may have run-outs (not tested till failure) above 1 million cycles. The minimum load is stress ratio (R) times the maximum load as in Equation 4.2. The usual stress ratios for research work are $R = 0.1$, $R =$ -1 and $R = 10$. The stress ratio chosen for the fatigue test was $R = 0.1$ as we are studying the tension-tension behaviour only.

$$R = \frac{F_{min}}{F_{max}} \tag{4.2}$$

A common testing frequency based on the literature is 2 Hz or 3 Hz [41]. In the present case, the testing frequency was set to 2 Hz and since the camera frame rate is 30 Hz, it was possible to capture 15 frames per fatigue cycle. The heat dissipated in low cycle fatigue is less than high cycle fatigue. So, if the test is successful in low cycle fatigue, it can be easily used for high cycle fatigue as well. However, a 1 Hz test frequency was neglected as it is slow and time consuming for a high number of cycles. The fatigue tests were load controlled which means that the test was controlled based on the force reference signal and the displacement response varied freely. The test was load controlled rather than displacement controlled because the loads will be reduced to maintain constant displacement in the later and this is not a suitable condition to measure the damage growth.

The steps followed to perform the fatigue test is explained below. The mounting procedure remains identical to the static test.

- The IR camera was mounted right in front of the test sample with the help of small fixtures.
- The IR camera was focused onto the area of interest and initially it was challenging as the temperature of the test sample was the same as the surrounding. Once the test started, a clear thermal image could be seen as the sample experienced thermoelastic heating.
- The camera was controlled by FLIR software interface via a computer. The camera started and stopped as per the predetermined interval. Example: 5 mins interval between each record.

- The test conditions were changed to load control for the fatigue test, the stress ratio and F_{max} were entered and the test was started.
- As soon as the test was started, the recording of the IR camera was also started manually through another computer. The subsequent starts and stops were controlled by a small piece of code.
- Since the IR camera and test controller were not synchronised, a small time gap of 2-5 seconds was observed. It should not be a problem as there was only a small mismatch of a maximum of 10 cycles.
- The test was undisturbed till failure. Sometimes, such tests run for hours or days or a week depending on the loads.

Figure 4.6 is the representation of S-N curves of the test samples tested under fatigue loading. The fatigue test was performed with eight samples. More details about the loads and the number of cycles are presented in Table 4.3.

.

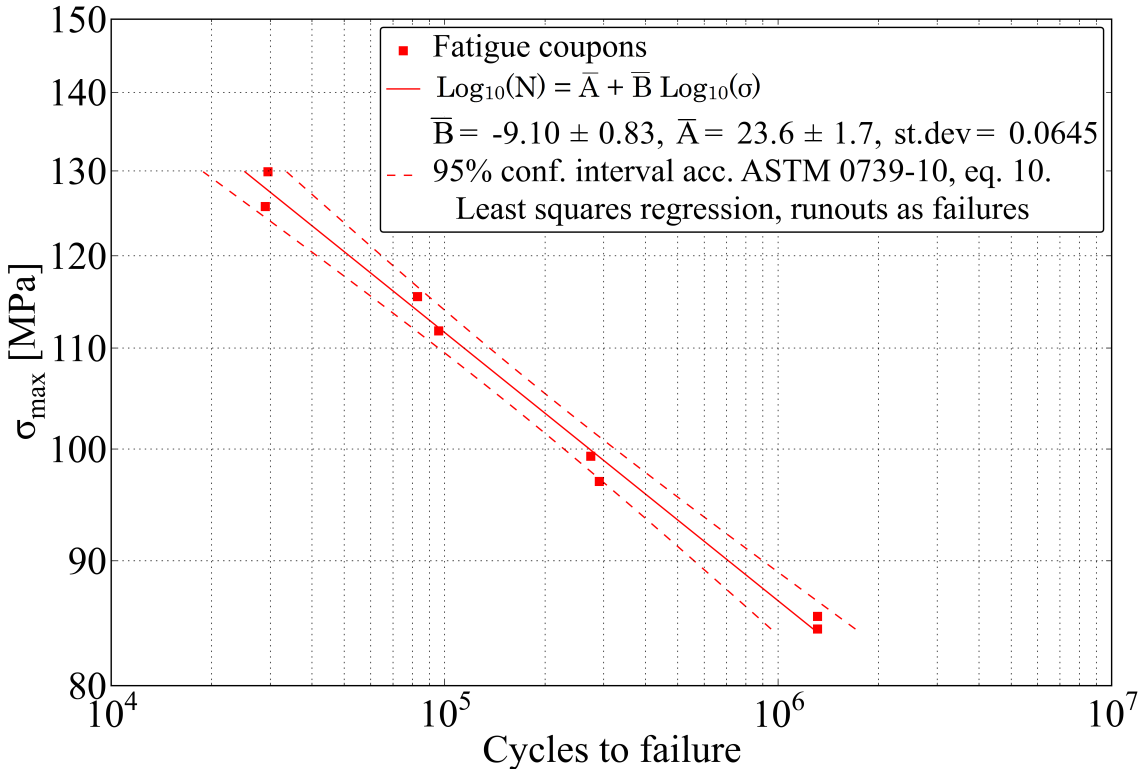

Figure 4.6: S-N curve of fatigue test performed

Figure 4.7 and Figure 4.8 are the images of the test sample before and after testing respectively. Figure 4.8 shows top view and side view of the failed sample.

Table 4.3: Fatigue test matrix, load ratio $[R] = 0.1$

Sample	% Load	No. of cycles $[N]$
WY-11	30	1,312,562
WY-12	30	1,313,678
WY-05	34	290,876
WY-06	34	274,280
WY-07	39	96,022
WY-08	39	82,900
WY-09	44	29,190
WY-10	44	29,056

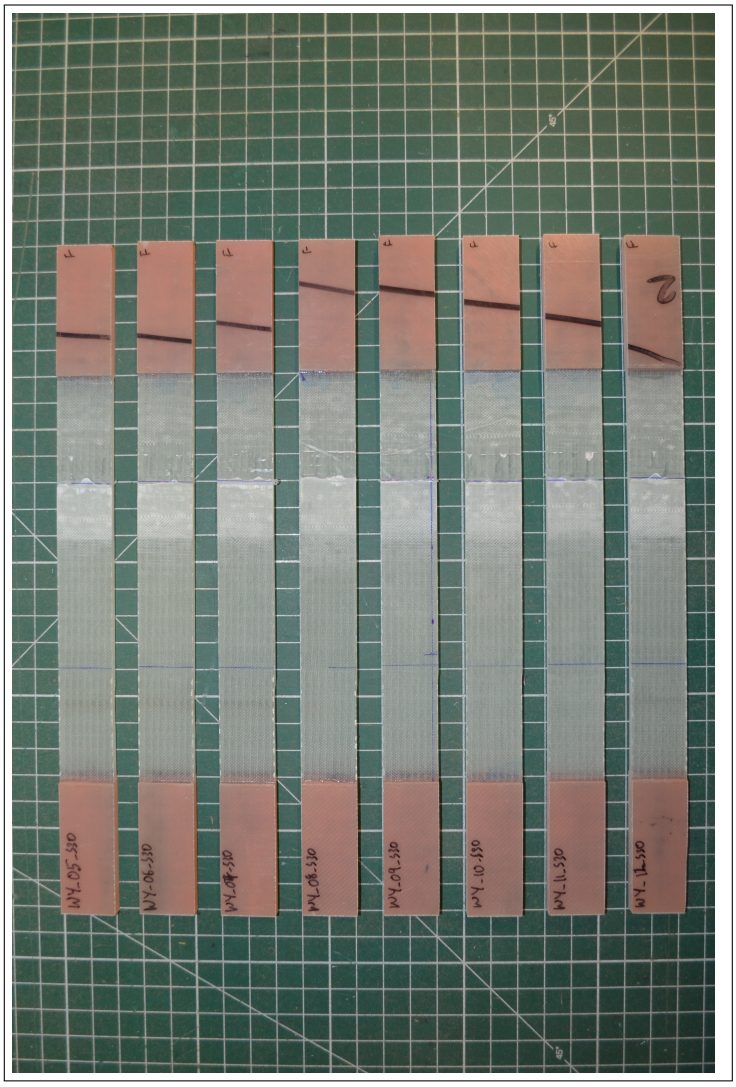

Figure 4.7: Image of the test samples before the test

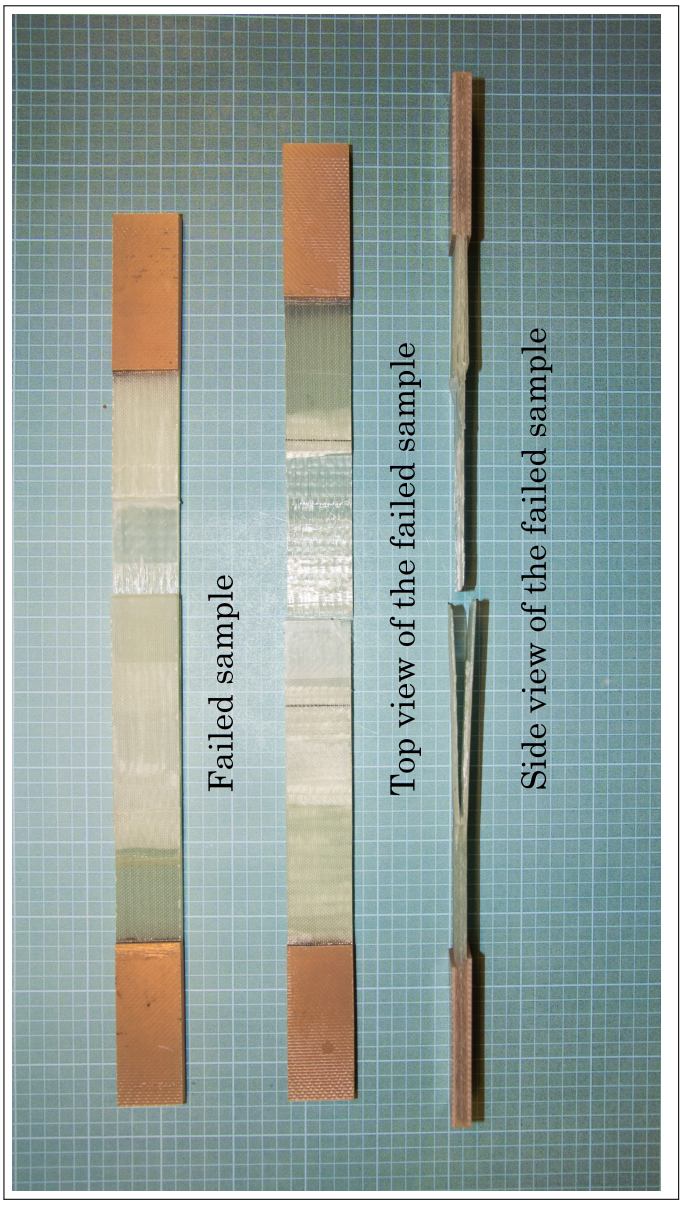

Figure 4.8: Image of the test samples after the test

This chapter concludes the experimental section of the research. The results from the static and the fatigue tests were explained in this chapter. From the test results explained in this chapter, it can be observed that the variation and deviation in the static maximum loads are small. This indicates that the samples showed similar behaviour and the anomalies due to manufacturing did not hamper the test results. Similarly in the fatigue test, the S-N curves were plotted without any abrupt behaviour. With this, it can be concluded that the experimental part was satisfactory. Now that the experimental part is finished, the next step is processing the thermal data captured during the test. The succeeding chapter describes the processing of thermal data.

Chapter 5

Infrared image processing techniques

Chapter summary *This chapter presents the reader with a comprehensive explanation of the processing techniques used to process the thermal images obtained during the experiments performed. The thermal images were essentially processed in two steps. Firstly, the thermal images were processed to eliminate noise and to get a detailed picture. Next, the processed thermal images were subjected to an image segmentation algorithm to evaluate the size of delamination which was the main area of interest of this research. Eventually, characterisation of delamination under fatigue loading was carried out.*

5.1 Causes for deterioration of IR images

In the recent years, the use of IR camera has gone beyond conventional applications like the military, medical fields and are extensively used as non-destructive tools for damage evaluation in structures. Also, the use of uncooled detectors has made the IR camera much cheaper and affordable. The IR images are always criticised for poor quality and low signal to noise ratio and this is significant in uncooled detectors. However, with modern computers, a lot of research has focused on noise reduction in IR images to enhance the adoption of IR technology [42–44].

There are several things that deteriorate the quality of the thermal images. In general, the thermographs are mainly deteriorated because of the following:

- Vignetting
- Fixed pattern noise
- Bad pixel or dead pixel
- Noise from the surrounding

5.1.1 Vignetting

Vignetting is an effect that displays a non-linearity in the thermal images making the centre of the image much brighter than the edge or corners of the image [45]. It is caused due to several reasons like pixel position and temperature variation with respect to the ambient. Vignetting is apparently one of the complicated issues to handle [45] as it is linked to the temperature of the surrounding with respect to the temperature of the lens and no effect is seen when both are at the same temperature.

Figure 5.1 is an example of a CPRF laminate designed with PTFE defect, Figure 5.1a is a CPRF laminate, Figure 5.1b is a thermograph with vignetting and bad pixels and Figure 5.1c is a thermograph with fixed pattern noise.

5.1.2 Fixed pattern noise

Fixed pattern noise (FPN) is an issue raised by the variations in responsivity of the detectors in an IR system to incoming irradiance [45]. This is a general difficulty faced while working with uncooled focal plane arrays (FPA) [45]. To an extent, the effect of FPN on image quality can be reduced by subtracting the image of a uniform scene from the image of interest.

5.1.3 Bad or dead pixel

A bad pixel can be described as an abnormal pixel behaving otherwise from the rest of the pixel array. For example, a dead or bad pixel stays OFF (black) although a hot pixel is ON (white) or vice-versa [46]. The bad pixels do not produce useful data in any way; they only contribute to worsening the image quality. A map of bad pixels is usually provided by the FPA manufacturer or they can also be recognised manually. Usually, to correct a bad pixel, the value corresponding to it is substituted by the average value of the adjacent pixels.

5.1.4 Noise from the surrounding

While the IR camera is focused onto the ongoing fatigue test, there will be a variety of thermal noise produced in the lab. The different sources of noises are 1) from the movement of people and machines, 2) noise from the reflection of the surroundings and 3) any data obtained by the IR camera other than the test frequency is also considered to be noise. The filtering of the signal at test frequency eliminates most of the noise from the signal and aids to get the desired signal output.

5.2 Recording procedure

Before diving into the processing techniques used to process the thermal images, more about the IR recordings has to be discussed. To monitor the delamination behaviour under the fatigue loading condition, certain measures are taken in this research. Firstly, to monitor the fatigue tests, it is impossible to capture a single image of the test sample without halting the test. Also, it was not a convincing idea to record the video for the entire test time because

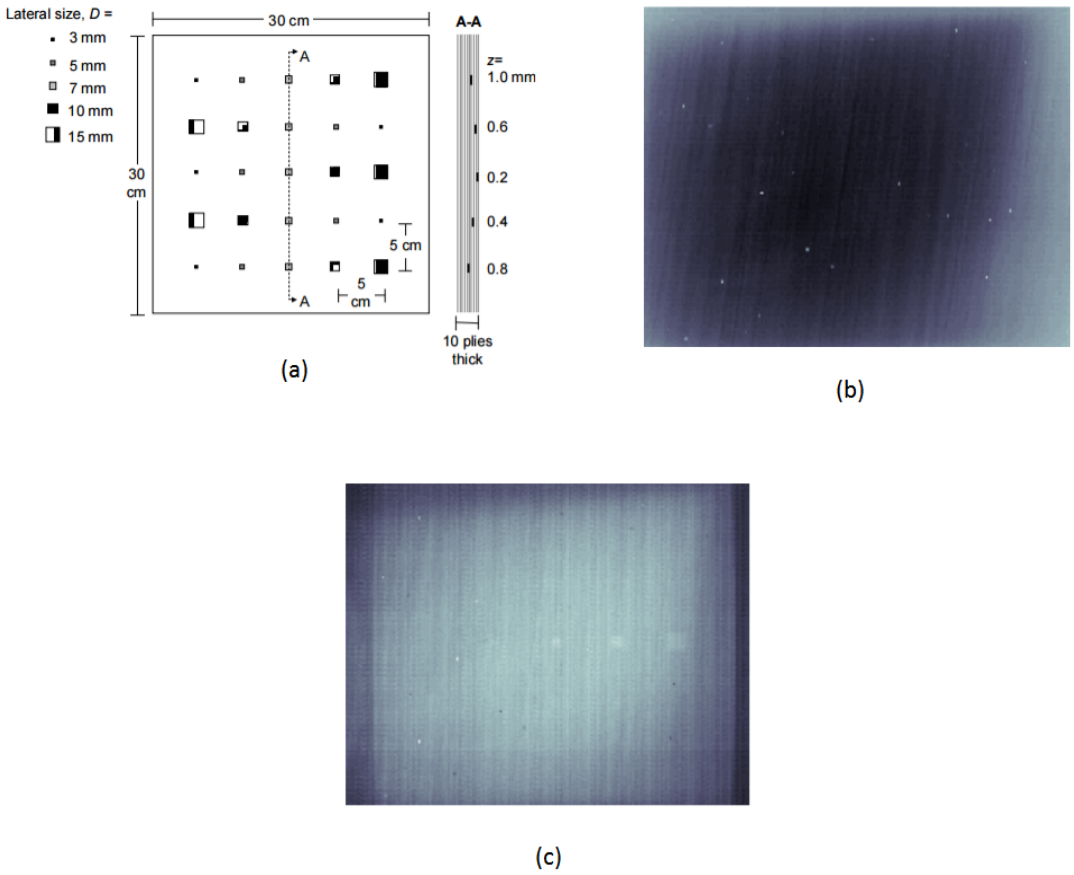

Figure 5.1: (a) CFRP laminate with 25 PTFE inserts as defect of different sizes and at different locations. (b) Raw image with vignetting and bad pixels. (c) Fixed pattern noise [47]

of space constraints and excess data to process. For example, if a test of 500,000 cycles has to be recorded with 2 Hz test frequency and 30 frames per second, the RAW 16 bit data will sum up to a mammoth total of 1.152 TB (see the calculation below).

There are 8 bits in a byte, so 16 bits per pixel implies 2 bytes per pixel, so the math is

- $320 \cdot 240$ pixels $\cdot$ 2 bytes per pixel $\cdot$ 30 frames per second = **4.608** MB/s
- Total data = 4.608 $MB/s \cdot 250000$ seconds (500000 cycles, 2Hz) = **1.152** TB

The enormous data is helpful but it turns out to be a real challenge to store and process the thermal data. The processing of thermal data in this case was not an easy process as the processing involved two steps (as shown in Figure 5.2). The entire process becomes very complex with the large data size. Therefore, to overcome this issue, short videos were captured with a certain number of frames at regular intervals of time during the fatigue test. In this case, the data captured would reduce in size and provide enough information about the fatigue behaviour. For example, in the above mentioned case, instead of recording for the entire length of the test, if the recording was done at every 10 minutes interval for 30

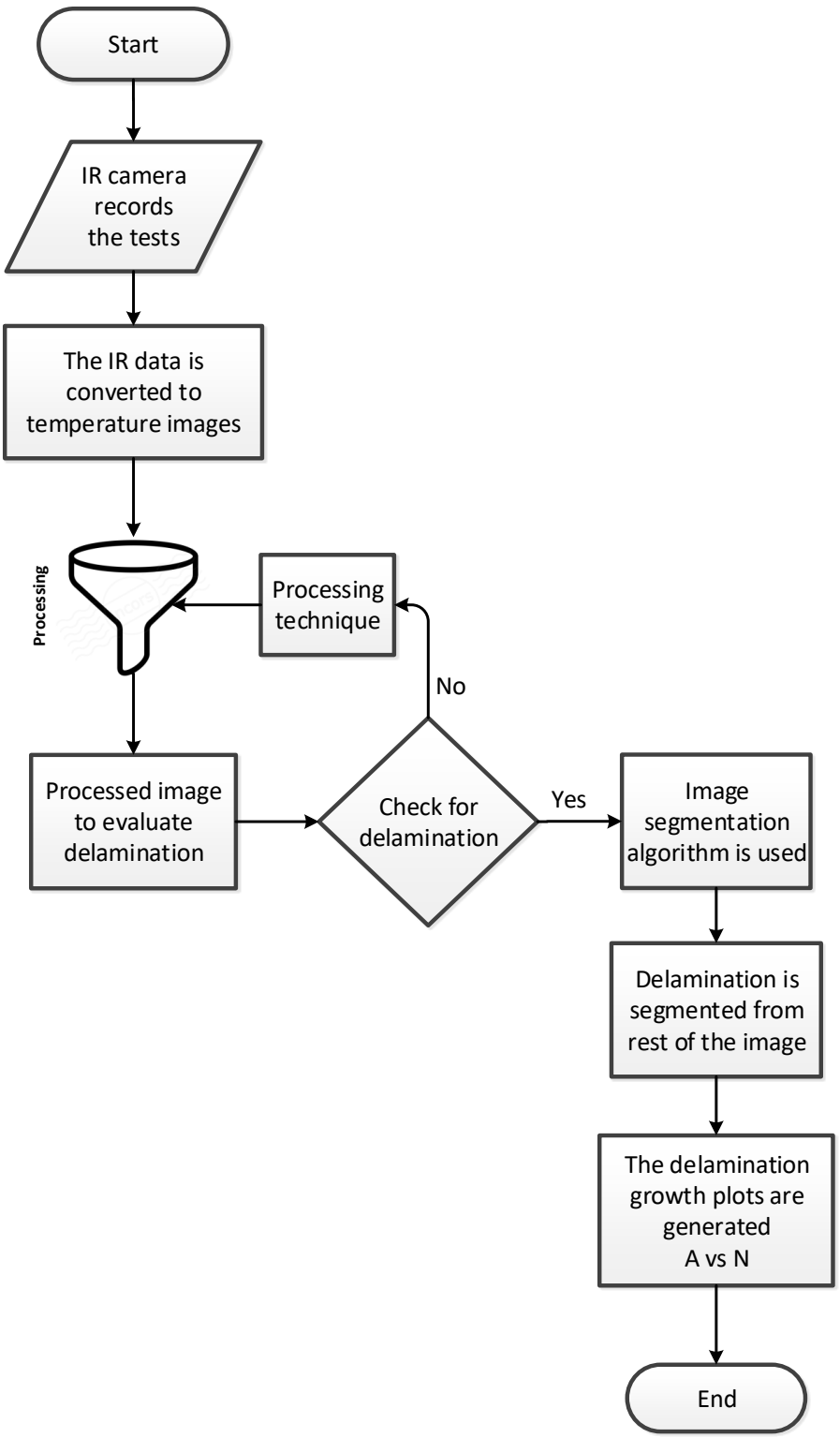

Figure 5.2: The approach used for processing thermal images

seconds. The total size of the recorded data will be 57.50 GB that is a great reduction in the data size and an acceptable range for processing. Moreover, the change in the delamination area or the delamination growth rate is quite negligible over a few number of cycles but it is very evident over 1000's of cycles. Thus, the selection of recording intervals with a gap of few 1000's of cycles is a good choice.

5.3 Different processing techniques

In this section, a brief discussion is made on several other techniques used for processing thermographs. While some of them are being used in practice, others are yet to be used for practical applications.

5.3.1 Thermal contrast

Thermal contrast is a simplistic operation that is based on temperature difference. Although there exists various definitions, all of them work on the same principle that is defined by the difference in temperature between the defective area and the sound area (non-defective area) [48], as in Equation 5.1.

$$\Delta T = T_d(t) - T_s(t) \tag{5.1}$$

Where, ΔT is the absolute thermal contrast, $T_d(t)$ is the average value of pixels in the defective area and $T_s(t)$ is the average value of pixels in the non-defective or sound area. The main disadvantage of thermal contrast technique is establishing the non-defective or sound area, especially if the process is automated [49], hence the thermal contrast technique cannot be used for this research.

5.3.2 Thermal signal reconstruction

Thermal signal reconstruction (TSR) [50] is a statistical technique which includes signal reconstruction from polynomials. This technique originated from the Fourier heat transfer equation on a semi-infinite plate that is subjected to thermal excitation. TSR works on the hypothesis that the temperature profiles for non-defective pixels follow the decay curve given by the one-dimensional solution of the Fourier equation, as represented in Equation 5.2.

$$ln(\Delta T) = a_0 + a_1 ln(t) + a_2 ln^2(t) + ... + a_p ln^p(t) \tag{5.2}$$

Thermal profiles belonging to non-defective areas in the sample will follow an almost linear decay, whereas the thermal behaviour of a defective area will deviate from linearity.

5.3.3 Principal component thermography

Principal component thermography (PCT) is a processing technique categorised under transforms. In this technique, the information from singular value decomposition is compactly extracted into spatial and temporal information of the image sequence using empirical functions. Singular value decomposition (SVD) is an eigenvector-based transform that forms an orthonormal space [50].

The SVD of an $M \times N$ matrix I (M>N) can be calculated as follows [51]:

$$I = \bar{U} L V^T \tag{5.3}$$

Where, $\bar{U}$ is an orthogonal matrix, L is a diagonal $N \times N$ matrix (with singular values of A present in the diagonal), V^T is the transpose of an orthogonal matrix.

5.3.4 Pulsed phased thermography

Pulsed phase thermography (PPT) is an interesting technique where the data is transformed from time domain to frequency domain using the one-dimensional discrete Fourier transform.

The thermal waves generated from the heated surface image can be detected remotely with IRT. Mathematically, a heating pulse can be decomposed into individual sinusoidal components of various amplitudes and frequencies. The tools like Fourier transforms can transform data from time domain to frequency domain and vice versa, see Figure 5.3 below.

The individual frequencies in PPT can be extracted by performing discrete one-dimensional Fourier transforms on each pixel of thermograph sequence using the mathematical Equation 5.4.

$$F_n = \sum_{k=0}^{N'-1} T(k) e^{\frac{2*\pi*i*k*n}{N'}} = Re_n + Im_n \tag{5.4}$$

Where, F_n is the one-dimensional discrete Fourier function, i is an imaginary number, k is the image index, N' is the total number of thermographic images, Re_n and Im_n are real and imaginary parts respectively and subscript n designates the frequency increment. The time evolution of each pixel in the field view is a vector T(k) for image sequence (n) is used to compute the real and imaginary parts. Amplitude Amp_n and phase ϕ_n are finally computed with Equation 5.5 below.

$$Amp_n = \sqrt{Re_n^2 + Im_n^2} \quad \text{and} \quad \phi_n = atan\left(\frac{Im_n}{Re_n}\right) \tag{5.5}$$

One limitation of using the Fourier basis function is that, they extend infinitely along the time axis meaning, no information can be obtained about the time evolution of spectral characteristics of the signal. In PPT, information about the location of damage is related to the time of observation as shown in Equation 5.6.

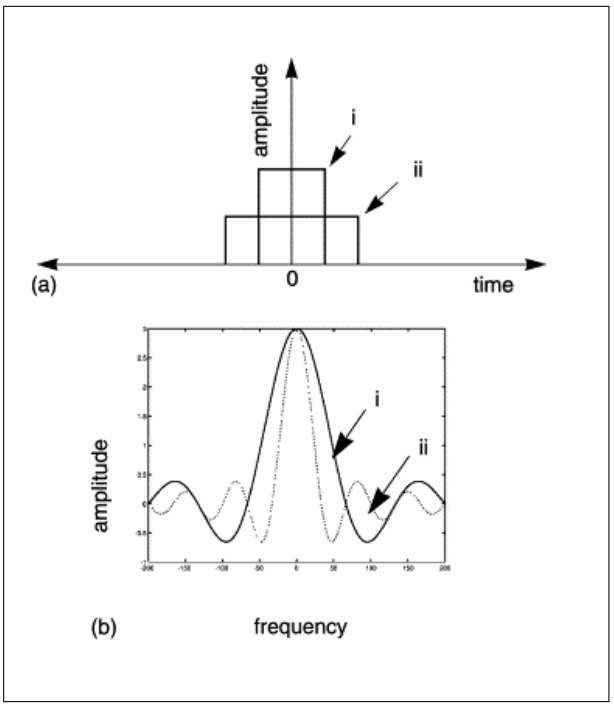

Figure 5.3: Time and frequency response (a) Two temporal pulses of (i) 15 ms and (ii) 30 ms duration, (b) Corresponding frequency spectra [52]

$$t = \frac{Z^2}{\mu} \tag{5.6}$$

Where, t is the time of appearance of damage, Z is the depth of inspection and μ is the thermal diffusivity of the material.

Pulsed phase thermography is the most commonly used transform technique and it is extensively used for several practical applications as explained in the previous section.

All the aforementioned processing techniques have their own pros, cons and render positive or negative results based on the type of image. Here, in this research, the images are recorded during the ongoing fatigue test; so, it is very important to choose a processing technique that can be used to filter the image at the test frequency as well. The best-suited technique to filter the image is fast Fourier transform (FFT) [53] [54] [55] [56].

The data recorded by the thermal camera during the test was processed in 2 steps as seen in the flow chart (see Figure 5.2). Before going into the processing technique, the recording and testing frequencies are mentioned again. The fatigue test is performed at 2 Hz, the IR camera is recording at 30 frames per second and at least 15 frames per cycle are captured.

The raw data recorded by the thermal camera is a sequence of temperature matrix represented spatially in time. Figure 5.4 represents a single frame in 2D and Figure 5.5 shows the data in 3D, the i and j axes represent the temperature data in 2D space whereas k axis represents the frames or image sequence.

The temperature matrix can be converted into a thermal image by assigning a colour map that looks like Figure 5.6 and in the same manner, the sequence of temperature image is

obtained. The first step of processing is to use PPT technique to transform the raw data from time to frequency domain that allows analysing the data from a different perspective.

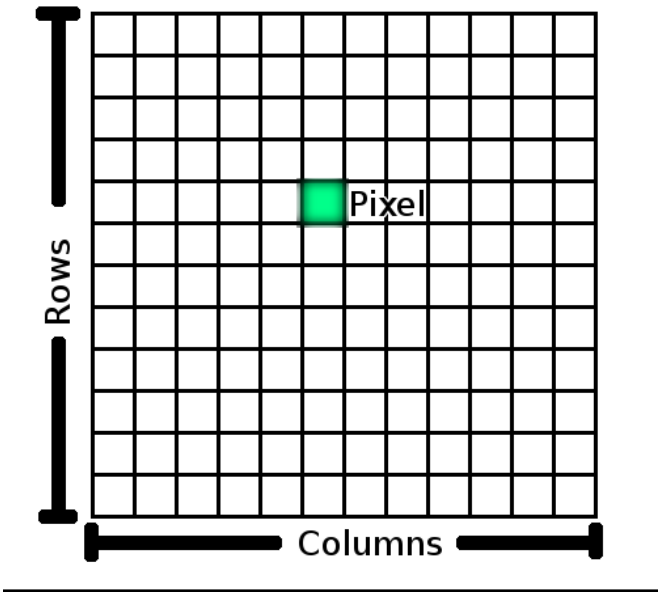

Figure 5.4: Representation of single pixel in 2D

The raw data consisted of a sequence of images of the temperature evolution T(t)(i,j) during the tests at each pixel (i,j) as in Figure 5.5. Amplitude and phase were computed at each pixel using a fast Fourier transform at fatigue test frequency of 2 Hz. The amplitude values were

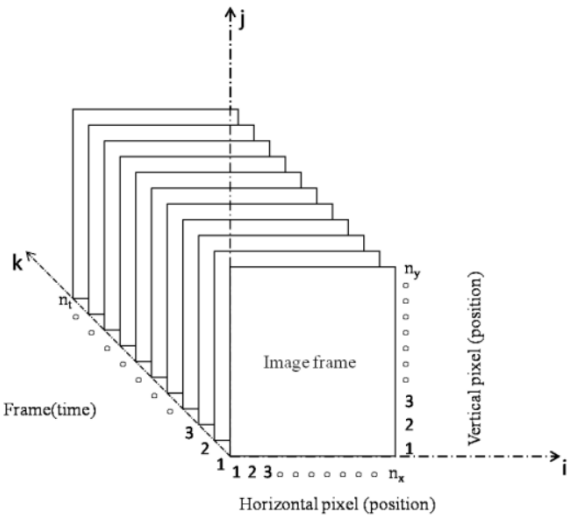

Figure 5.5: Representation of several frames over time in 3D

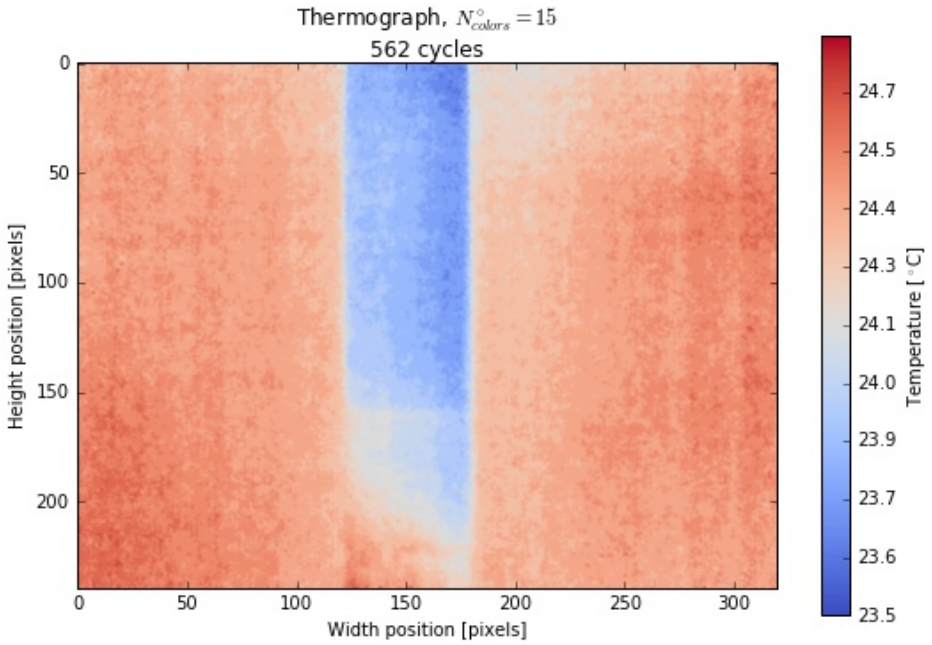

Figure 5.6: Temperature plot with colour map

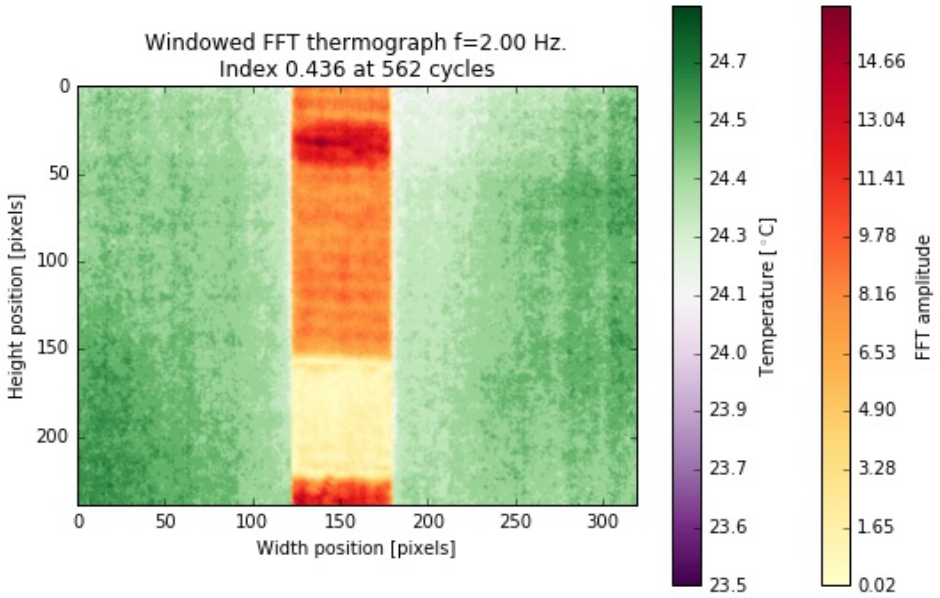

Figure 5.7: Amplitude plot with colour map

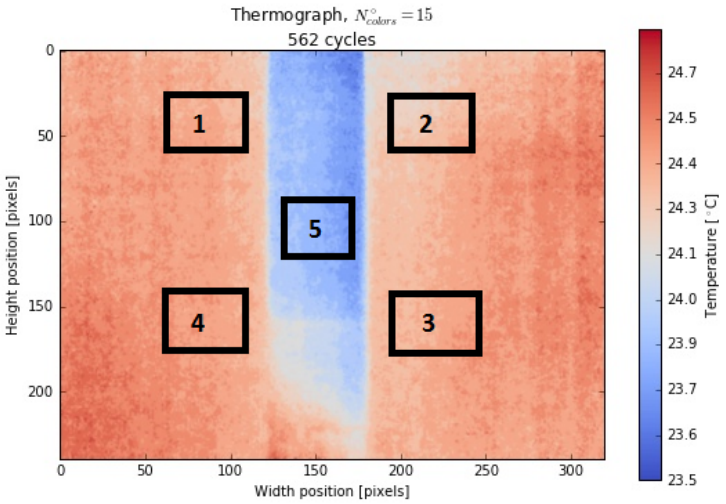

Figure 5.8: Selection of locations for SNR calculation in temperature image

plotted with colour maps to obtain FFT thermographs as in Figure 5.7. The ampligraphs are further processed using an image segmentation algorithm to segment them into different regions like delaminated and un-delaminated regions. More about segmentation is discussed in Section 5.5.

Before proceeding into segmentation, a small test was conducted to check the quality of the processed image. As discussed earlier, the thermal images were criticised for poor signal to noise ratio (SNR). So in the next section, the signal to noise ratio values of the thermal image before and after processing are checked and verified if the signal quality has increased after the processing.

5.4 Signal to noise ratio

Signal to noise ratio is a parameter used in image processing as a measure of sensitivity of an image. Often signal to noise ratio is written as S/N or SNR, it is a ratio of signal strength corresponding to background noise. The ratio is normally measured in decibels (dB) using a signal to noise ratio formula as in Equation 5.7. If the incoming signal strength is V_s and the noise strength is V_n, then the signal to noise ratio, in decibels, is given by the formula:

$$SNR = 20 \cdot log \frac{V_s}{V_n} \tag{5.7}$$

Where, V_s is the signal strength, V_n is the noise strength and SNR is the signal to noise ratio expressed in decibel. If signal strength V_s = noise strength V_n, then SNR = 0. In this condition, the signal becomes unreadable since the noise level seriously competes with the signal. Ideally, V_s is more than V_n. So a high ratio of signal to noise can be obtained. Therefore SNR will be positive.

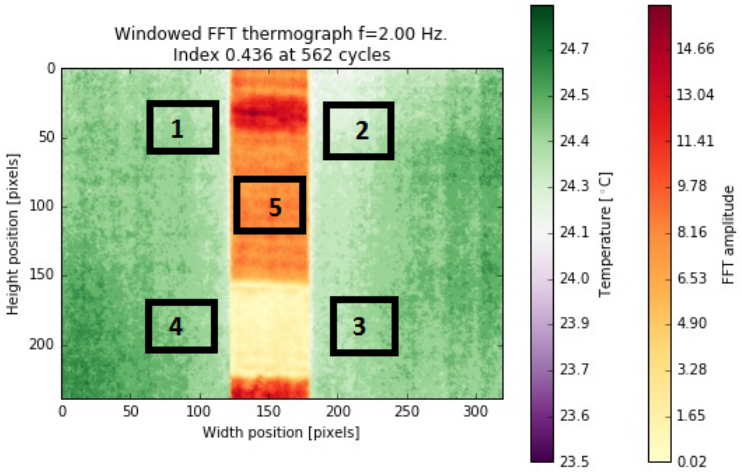

Figure 5.9: Selection of locations for SNR calculation in processed image

Table 5.1: SNR values

Samples	**SNR** (dB)
Temperature image	9.29
Processed image	20.27

To perform SNR analysis for the current research, the SNR values of the actual temperature images and processed FFT images are compared. The comparison will give an idea about the change in SNR values before and after processing. To perform a fair analysis, different locations of the sample are chosen to compute SNR and Equation 5.8 is used for this analysis.

$$SNR = 20 \cdot log \frac{(Max_{intensity} - Min_{intensity})_{object}}{(Mean_{std})_{surrounding}} \tag{5.8}$$

Here, the (Max&Min $_{intensity})_{object}$ is obtained from the location 5 and the $(\text{Mean}_{std})_{surrounding}$ is obtained from the locations 1 to 4 as shown in Figure 5.8 and Figure 5.9.

The SNR values are published in Table 5.1. It can be clearly seen that the SNR value has drastically increased in the processed image. So it can be said that the processing technique used has served the purpose.

Once the images are processed, the next step is segmenting the processed images.

5.5 Image segmentation

Image segmentation is a process of separating an image into various segments. These segments can be represented in different ways so that only the area of interest is targeted making it more meaningful and straightforward to analyse. Here, in this research, once the thermal

images are processed, the images are segmented to segregate the delaminated region from the rest of the image so that the delamination growth rate can be studied.

The major segmentation techniques are :

- Segmentation by edge detection
- Segmentation by thresholding
- Segmentation by region
- Segmentation by feature-based clustering

5.5.1 Segmentation by edge detection

Edge detection technique segments an image by identifying the edges or pixels connecting various regions that have a rapid change in intensity. These pixels are extracted and joined to make a closed counter and the outcome is a binary image [57]. Based on the theory, there are two main edge based segmentation methods, namely, grey-histogram and gradient-based method.

5.5.2 Segmentation by thresholding

Thresholding technique is the simplest method to segment an image based on the intensity value that is called threshold value. The main advantage of this technique is that it can be applied locally and globally [57]. The global thresholding is used to distinguish the object from the background by the given threshold value and local thresholding is used to sub-segment the image based on the local characteristics.

5.5.3 Segmentation by region

Segmentation by region is also known as similarity based segmentation because this technique works by grouping the pixels belonging to the same object [58]. The advantage of this technique is that there won't be any gaps due to the missing pixels at the edges because once the change in colour or texture is identified, the edge flow is converted into vectors and further segmented based on the vector.

5.5.4 Segmentation by clustering

A cluster is a group consisting of similar pixel belonging to a specific region which is different from rest of the image. Clustering is a process of arranging the groups based on their attributes. There are several clustering techniques used, out of which, the most popularly used are K-means and fuzzy C-means algorithms.

On compiling all the techniques [59], it is stated that edge detection yields best results for the images with finer features. Thresholding is best suitable for images with fewer features.

Region based technique separates the image based on the local feature in the image and clustering technique segments the image by colour features in the image. Segmentation performed on an image using all the techniques showed that region based and thresholding methods gave better results [59] but it is unfair to compare all the techniques on the same image as every technique is unique and has their own pros and cons. An overview of the techniques is provided in Table 5.2.

Table 5.2: Comparison of various image segmentation techniques [60]

Segmentation technique	Brief description	Advantages	Disadvantages
Edge detection	Based on discontinuity or rapid change in pixel intensity	Works good on images with better contrast	Not suitable for images with lot of edges
Threshold method	Division based on pixel intensity levels	Easy and simplest method. Best suitable for images with fewer features.	Highly dependent on pixel intensity
Region based	Partitioning based on the homogeneity in the images	More immune to noise, easy to define similarity criteria	Time consuming method
Clustering	Division based on homogeneous cluster	More useful for complex images mostly in medical images	The function is complicated

In this research, thresholding method is used for image segmentation. The thresholding method is the simplest technique and best suited for the image sample with fewer features [59]. This method is also suitable for the images having lighter objects than the background. From Figure 5.7, it can be seen that delamination in the image is lighter compared to others in the image.

To perform image segmentation on the images obtained from processing the thermal data as mentioned in Section 5.3, a threshold value has to be selected. The threshold value can be selected manually or automatically based on the image to be segmented. There are basically three ways to select the threshold value [59] [61].

1. Global thresholding: The global threshold is performed by selecting an appropriate threshold value Thr [57]. The value of Thr will remain constant for the entire image. On the basis of Thr value chosen, the output image $g(i,j)$ is produced from original image $f(i,j)$ as:

$$g\,(i,j) = \begin{Bmatrix} 1\text{,if f(i,j)} > Thr \\ 0\text{,if f(i,j)} \leq Thr \end{Bmatrix}$$

2. Variable thresholding: In the case of variable thresholding, the value of Thr will vary over the range of an image [57, 58]. This can be further classified into two types: Local threshold: In this, the value of Thr depends on the neighbourhood of i and j. Adaptive threshold: The value of Thr is a function of i and j.

3. Multiple thresholding: In the case of multiple thresholding method, there are several threshold values like $Thr0$ and $Thr1$. By using these, the output image can be calculated as:

$$g(i,j) = \begin{Bmatrix} 0,\text{if f(i,j)} > Thr1 \\ 1,\text{if f(i,j)} \leq Thr1 \\ 2,\text{if f(i,j)} \geq Thr0 \end{Bmatrix}$$

To segment the image in this research, a global threshold value was used. The threshold value was selected manually and remained constant for all the images.

Figure 5.10 shows an image segmented with a contour. Once the segmentation is done, the next step is to calculate the number of pixels in the segmented portion. The number of pixels in the segmented portion provides geometrical information such as area, perimeter, etc. Once the number of pixels is known, the pixel count is multiplied by a conversion factor so that the area in SI unit can be calculated. For example, Figure 5.10 shows segmentation and number of pixels enclosed.

Once the image has been segmented, the number of pixels in the segmented region can be easily obtained. The known pixel count is multiplied with a pixel conversion constant to convert it into the area which is nothing but the delamination area.

An example is shown here to evaluate the pixel conversion constant. Consider Figure 5.10, the width 20 mm is made up of 10 pixels so that the length of each pixel will be:

$$\text{Pixel constant} = \frac{\text{width or length}}{\text{number of pixels}} = \frac{20}{10} \tag{5.9}$$

$$= \mathbf{2}\ mm$$

Thus, the area of each pixel will be,

$$2 \times 2 = \mathbf{4}\ mm^2$$

40 pixels are enclosed in the contour. so,

$$40 \times 4 = \mathbf{160}\ mm^2$$

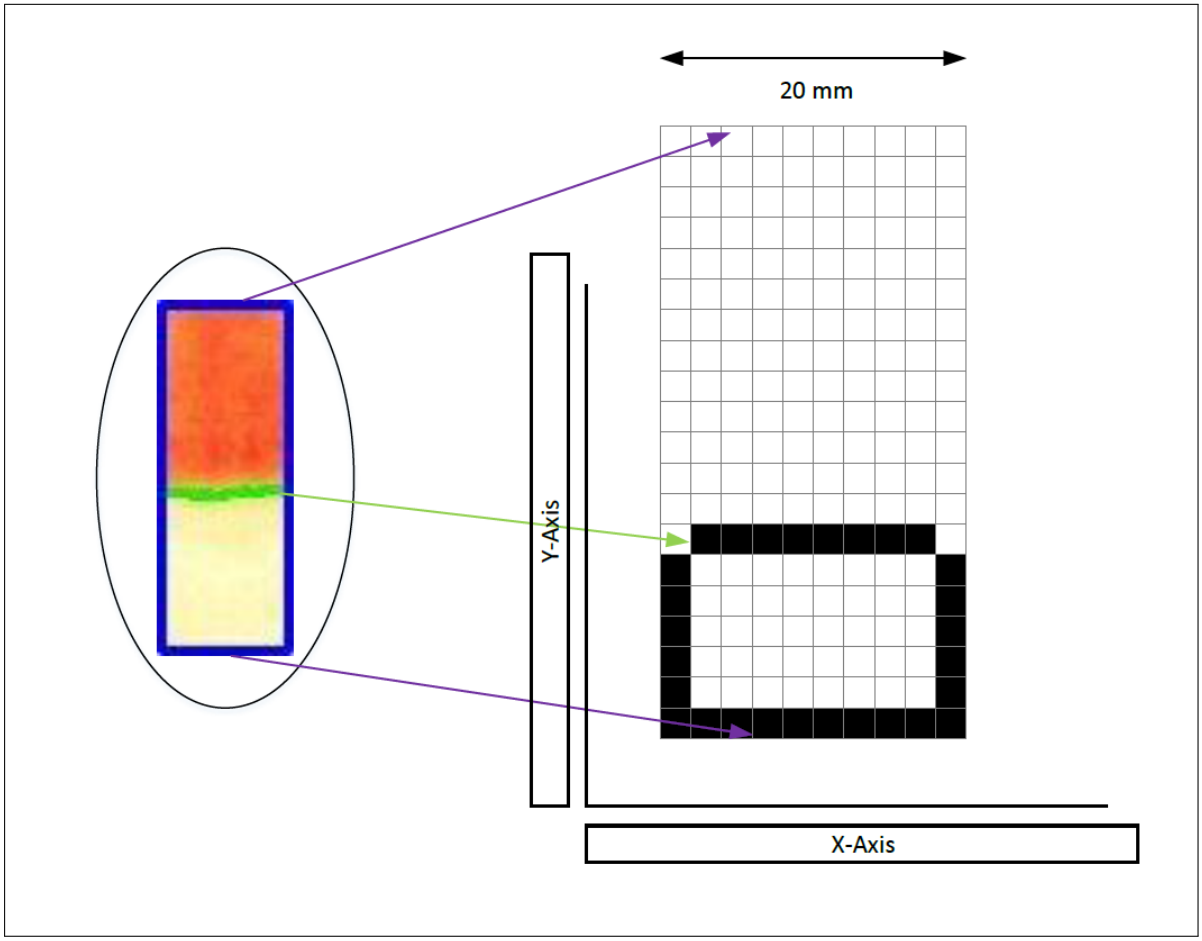

Figure 5.10: Representation of single pixel in 2D

To conclude, this chapter explains the processing technique used for processing the thermal images. The processing technique used seems to be satisfactory with the SNR values calculated for the images before and after processing. Later, the image segmentation process is explained which is used to segment the delamination and study its behaviour under fatigue loading. This chapter also concludes the processing section of the research. Now results has to be discussed which is done in the following chapter.

Chapter 6

Test results and discussion

Chapter summary *This chapter is dedicated to results and discussion. The findings from both the experimental section in Chapter 4 and processing section in Chapter 5 are discussed. In the first section, the discussion is based on the experimental results, a later section covers the discussion on thermal data analysis. Finally, findings from the thermal data are critically evaluated and compared with the visual light camera data and a decision is made on the possible errors in the calculation.*

6.1 Experimental results

The static and the fatigue tests results are published in Table 4.1 and Table 4.3 respectively in Chapter 4. From the static test, it can be noted that the maximum stress was found to be 272.18 MPa with a variation of 0.042% over a sample size of four. All the samples failed in the similar fashion with the same magnitude of loads. It was observed that the variation due to manufacturing was less and hence had no effect on the maximum load, also the results showed good repeatability.

The fatigue tests were conducted approximately at 30%, 35%, 40% and 45% of maximum static load with the stress ratio of $R = 0.1$, for all the samples. The fatigue tests were monitored using the IR camera, to capture the delamination area. S-N curves are plotted from the obtained fatigue test data as shown in Figure 4.6. The plot clearly indicates that the test followed a linear trend with less scatter with no abrupt behaviour. From this, it can be stated that the manufacturing of the test sample with defect and the testing conditions did not produce any unintended behaviour.

When the static load was applied, the sample majorly experiences shear force. The sample has a double shear configuration as discussed in Section 3.3, the maximum static load mainly depends on the shear area. However, it is a different case during fatigue loading because the 1st and the 4th layer start to delaminate, with the PTFE insert being the initial delamination

point. Delamination is the predominant failure mode as it experiences both mode 1 (opening) and mode 2 (shear) loads as shown in Figure 6.1. The matrix that is filled in the space between cut fibres in location 2 also starts to crack but the damage growth on the external plies is faster. As the delamination is faster, it becomes the predominant failure mode and all the samples in this experiment failed because of delamination.

Figure 6.2 shows the approach of this research according to which, the research is divided into two major sections, the experimental section and IR monitoring section. The experimental section is concluded by evaluating the strain energy release rate. The IR section consists of capturing the thermal data during the test and concluded by evaluating the delamination growth rate curves. Finally, a comparison test was conducted to compare the data obtained from the thermal camera with that from the visible light camera. The fracture mechanics based approach connects delamination growth to the fracture mechanics concept of strain energy. The strain energy is calculated with the help of data from the test machine. Typical test data from the test looks like the data in Figure 6.3. The maximum strain energy U_{max} is given by Equation 6.1.

$$U_{max} = \frac{1}{2} \times F_{max} \times \delta_{max} \tag{6.1}$$

Where, F_{max} is the maximum force and δ_{max} is the maximum displacement obtained from the test machine. The strain energy from the test machine was plotted against the number of cycles as in Figure 6.4. Further, the strain energy release rate, ΔG_{max} of each sample was deduced from the slope (dU_{max}/dN) of the curves in Figure 6.4.

From Figure 6.4, it is clear that the strain energy release rate for higher loads is higher and for lower loads remains lower. The samples with similar loads have almost identical strain energy release rates except for the 35% load case i.e. green and red lines. Even though they both have same loading conditions, they exhibit different strain energy release rate. By observing keenly, it is inferred that both have the same trend with just an offset. So, it is assumed that there is some kind of error in the measurement, mostly an offset in the displacement measurement.

By knowing the error in measurement, if was decided to correct the error. The strain energy release rate plot will change as seen in Figure 6.5 where the 35% loading plots green and red are almost overlapping obeying the condition that the strain energy release rate will remain the same for a given loading condition.

6.2 Processed thermal data

The thermal response of the samples were captured continuously for the change in temperature for the complete life cycle of the sample at certain intervals. The signal recorded by the IR camera is not purely the signal from the test sample as it also includes the noise from the surrounding. The signals from the actual tests were at a frequency of 2 Hz which is different from that of noise. So, the data obtained was processed by filtering the noise in the frequency domain with the help of fast Fourier transform. The amplitude and phase were extracted at each pixel for every image over the entire fatigue life and amplitude plots were generated.

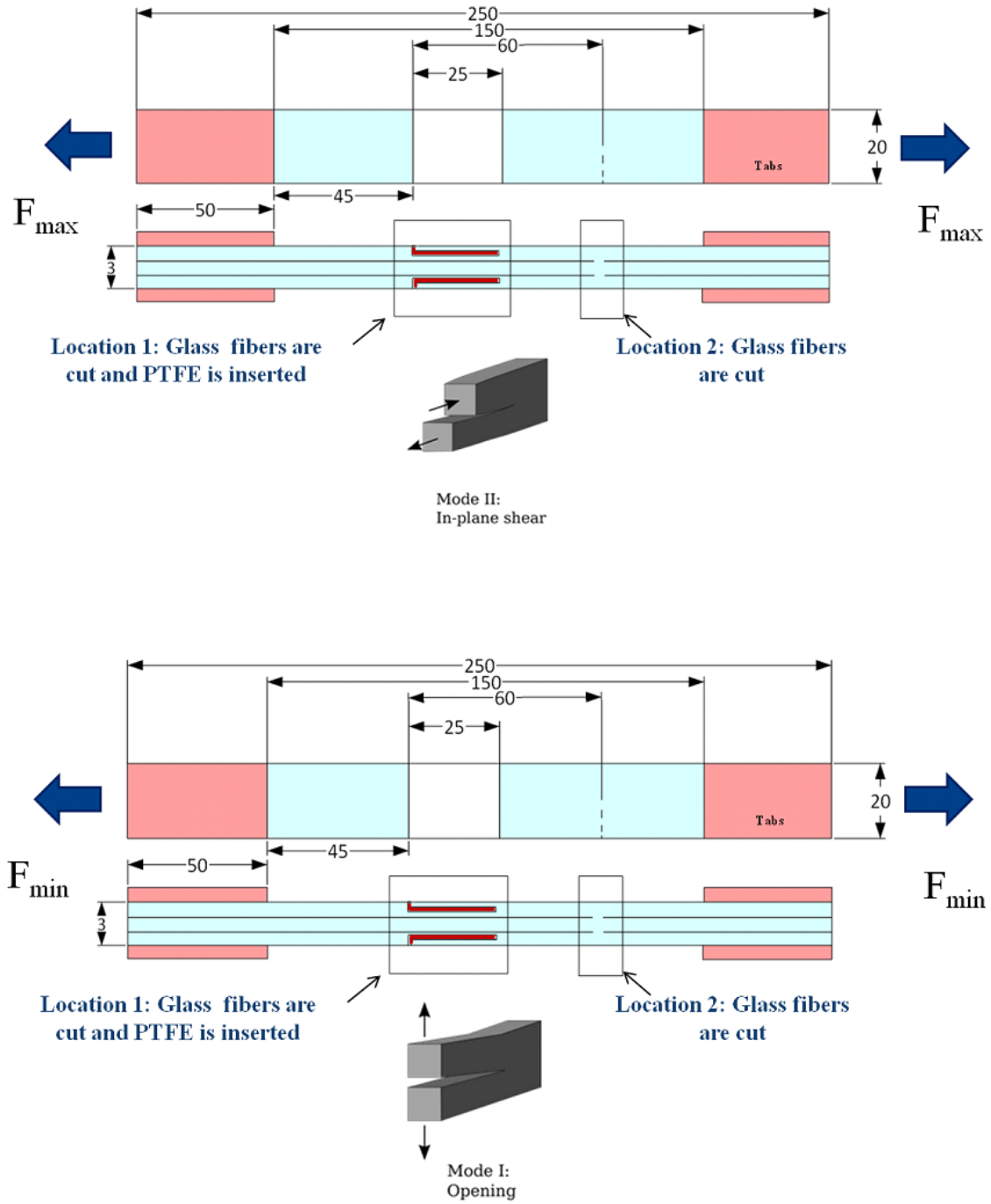

Figure 6.1: Type of failure during F_{max} and F_{min} loads. All units are in mm

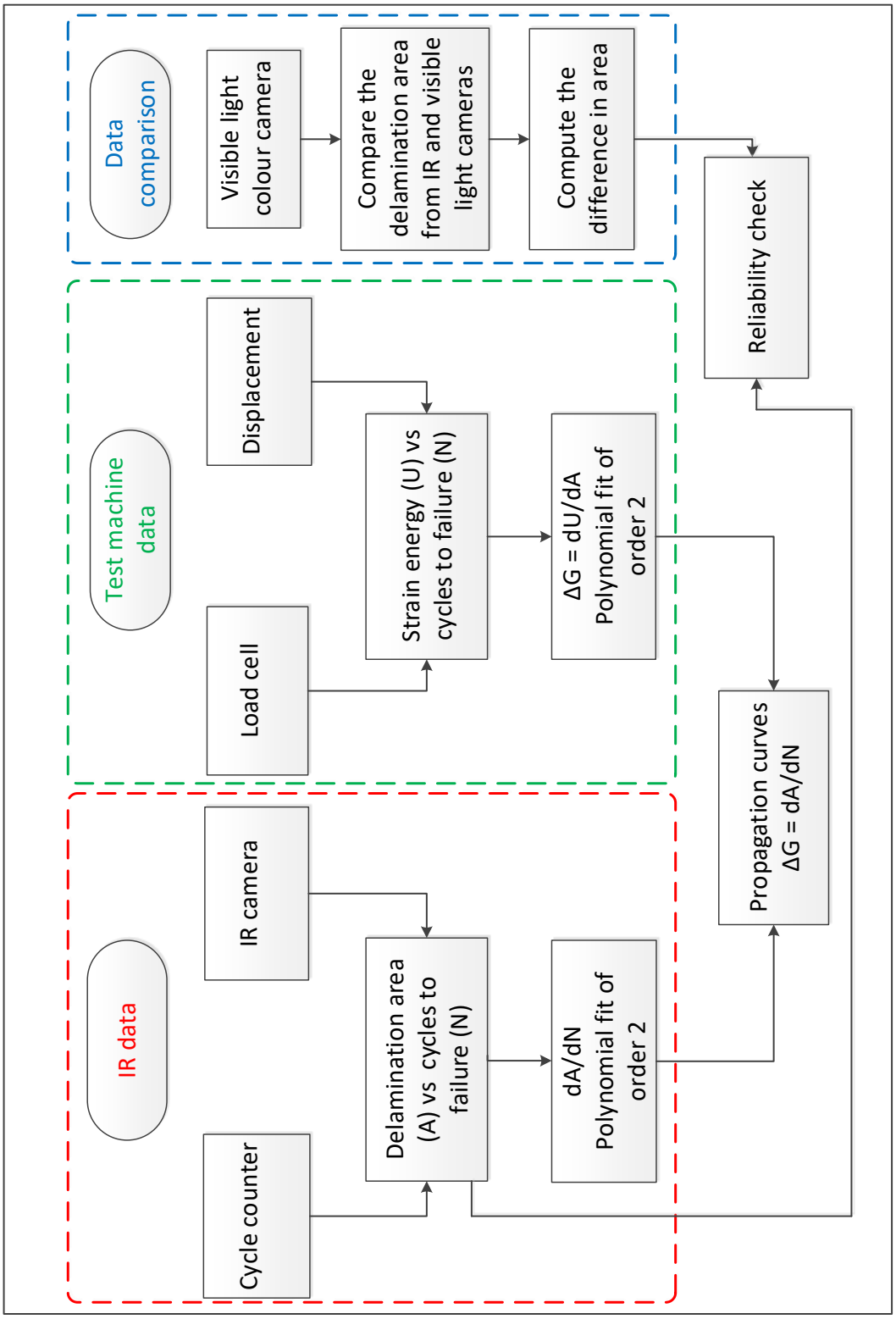

Figure 6.2: The flow chart of the research, consolidating all the sections

Test results for specimen: WY_10_S30

N_{max}	R	Area [mm^2]	Num. buf	Freq. [Hz]
29802	0.1	75.2	20 [400]	2.0
$N_{max-log}$	Run-out	Gauge [mm]	Pto/cycle	Sampling rate
29000	False	148.9	400	800 Hz
Bending	Poisson 1	Poisson 2	E1 [GPa]	E2 [GPa]
nan	nan	nan	nan	nan

Channel	Mean	Max	Min
Force [kN]	5.2	9.4	0.9
σ [MPa]	69.1	125.7	12.6
δ [mm]	0.72	1.21	0.23
Temp. ambient [C]	23.6	23.6	23.6
Temp. coupon [C]	37.0	37.0	36.9

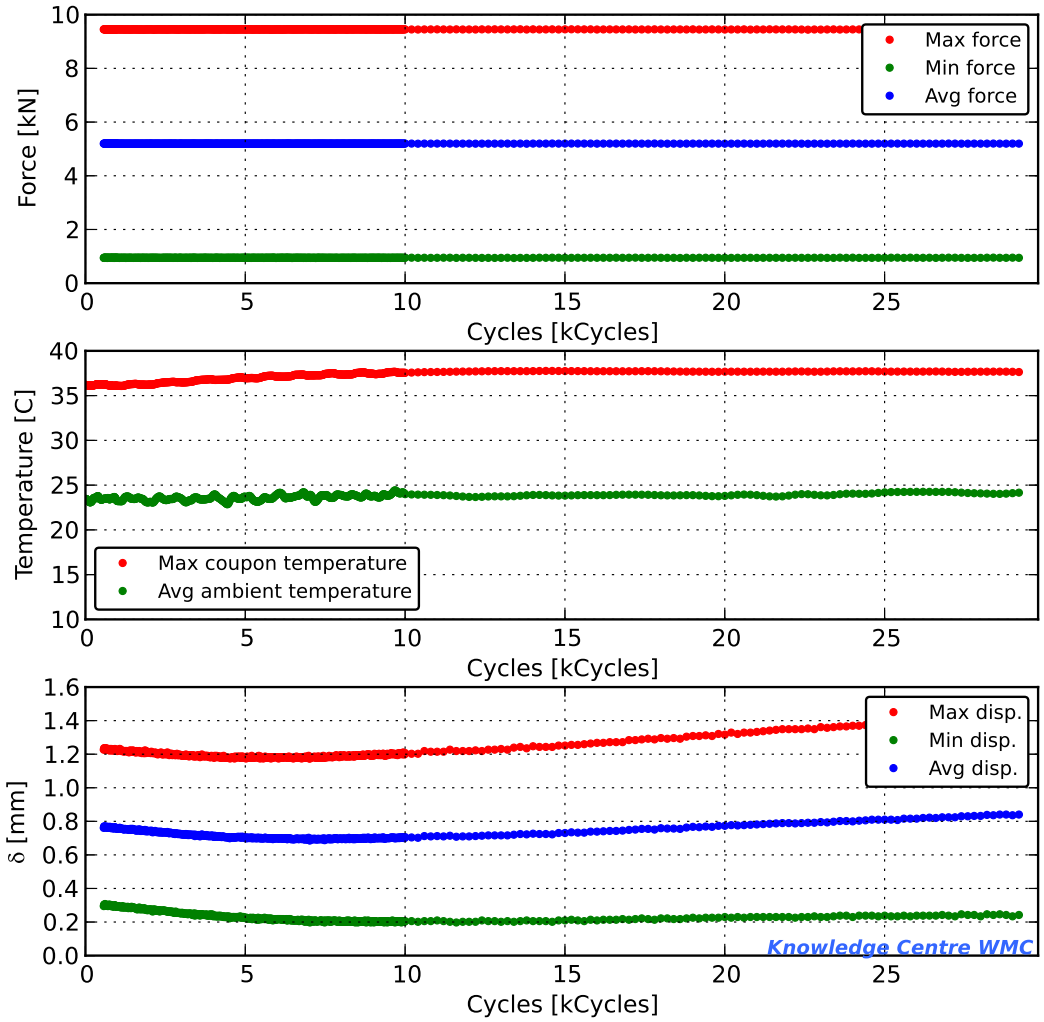

Figure 6.3: A typical test data record sheet from the test machine

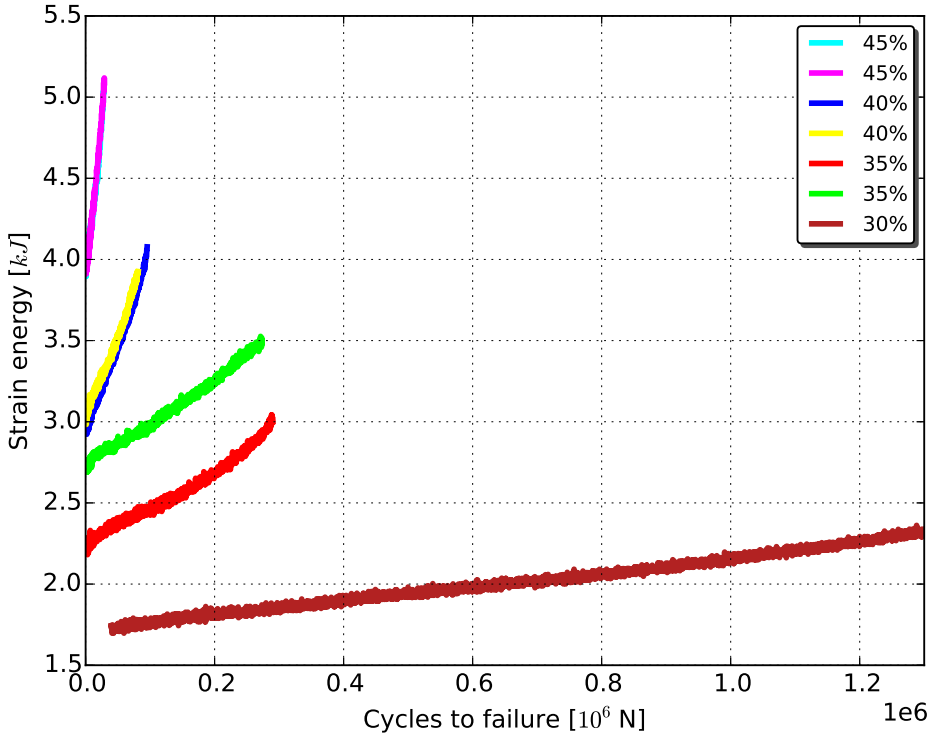

Figure 6.4: Strain energy vs cycles

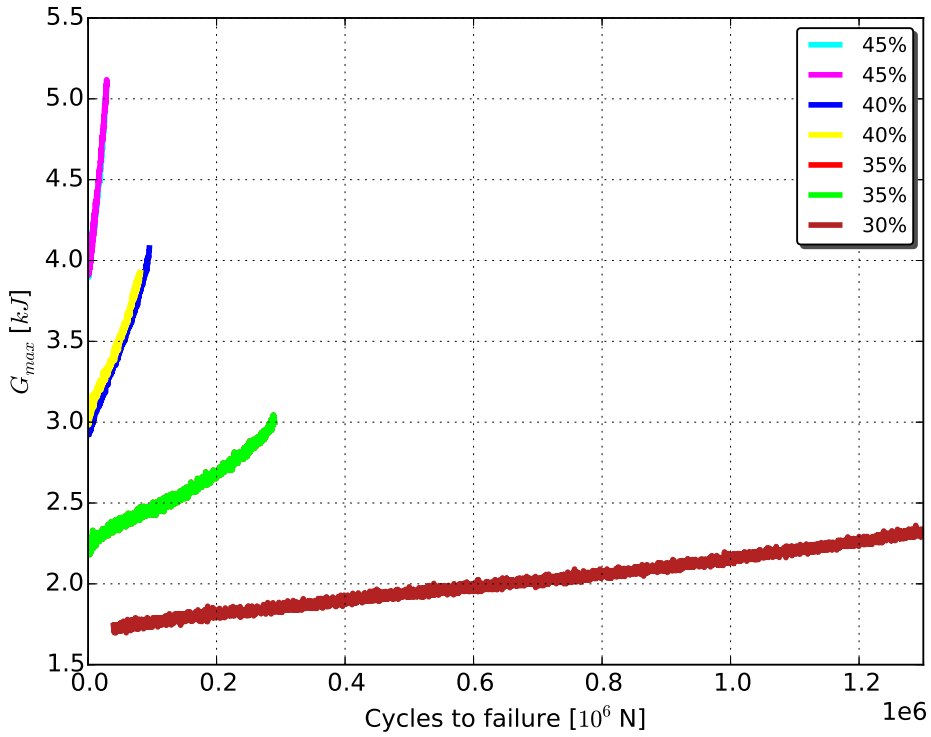

Figure 6.5: Corrected strain energy vs cycles

Further, the amplitude plots were processed using the developed image segmentation algorithm to obtain the delamination area based on the amplitude values. Knowing the delamination area at a given number of cycles allowed the delamination growth rate curves A vs N to be obtained, as shown in Figure 6.8. To arrive at the delamination growth rate plots, the delamination should be calculated at various cycles during the test. Figure 6.7 provides the complete picture of delamination and sub Figures (6.6a - 6.6z) show the delamination at various cycles. The images belong to 45% load case and the green line represents the crack front in the test sample.

From Figure 6.8, it is seen that the delamination growth in all the samples follow curves with different average slope. The samples with higher stresses (for example WY-09, 45%, cyan color) undergo a faster rate of delamination, whereas the lower stress samples (for example, WY-12, 30%, brick color) display slow delamination rates. It is also seen that the delamination growth curves show three distinct regions, namely, the threshold region, the linear region and the fast fracture region as seen in the literature [62].

The strain energy obtained from the test machine is plotted against the number of cycles as in Figure 6.4. The slope from Figure 6.4 gives the strain energy release rate ΔG i.e. (dU_{max}/dN).

This space is intentionally left blank

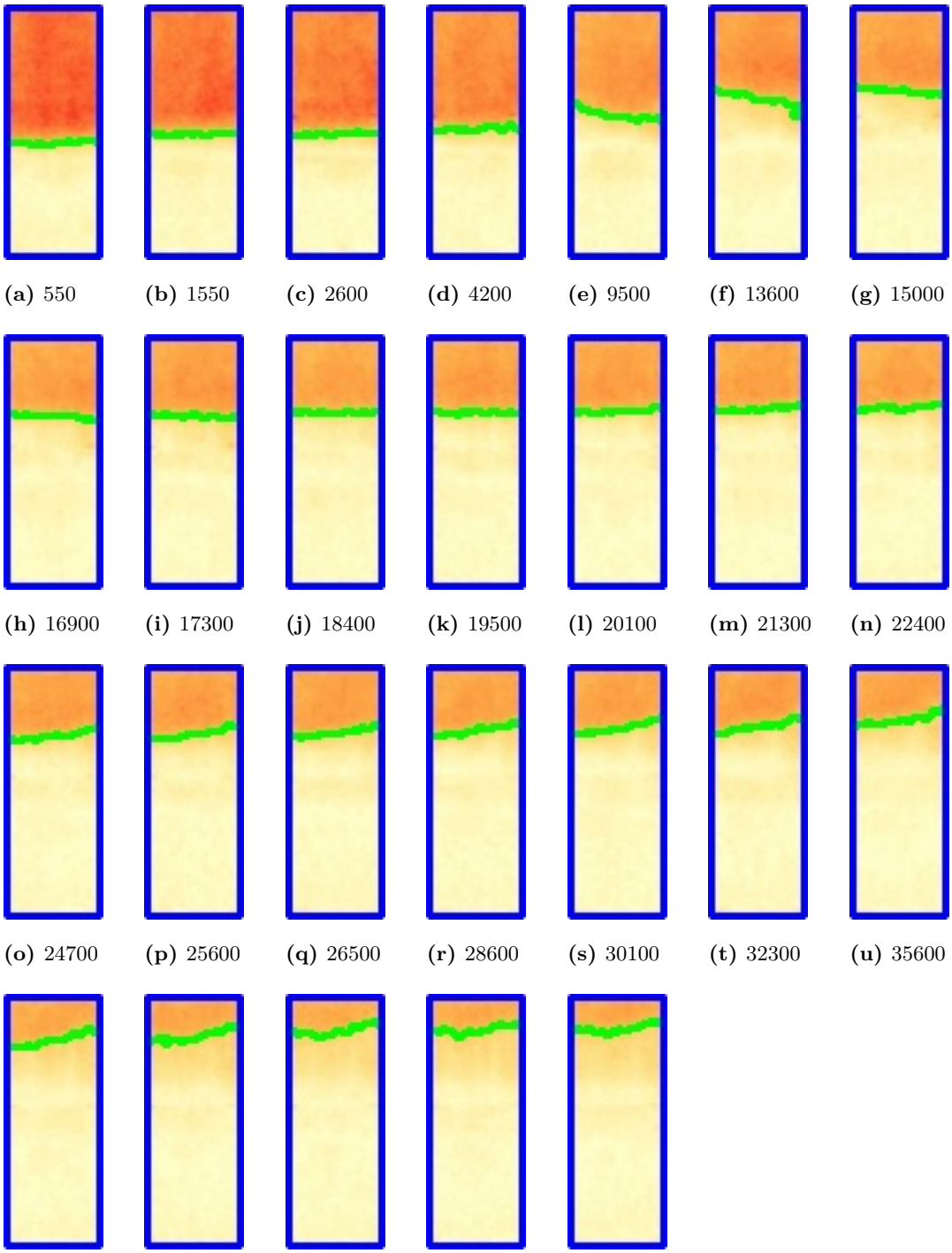

(a) 550 (b) 1550 (c) 2600 (d) 4200 (e) 9500 (f) 13600 (g) 15000

(h) 16900 (i) 17300 (j) 18400 (k) 19500 (l) 20100 (m) 21300 (n) 22400

(o) 24700 (p) 25600 (q) 26500 (r) 28600 (s) 30100 (t) 32300 (u) 35600

(v) 38500 (w) 40000 (x) 41800 (y) 43300 (z) 44000

Figure 6.7: The tracking of delamination at various cycles, the green marking represents the crack front. The darker region is the undelaminated region and the lighter region is the delaminated region

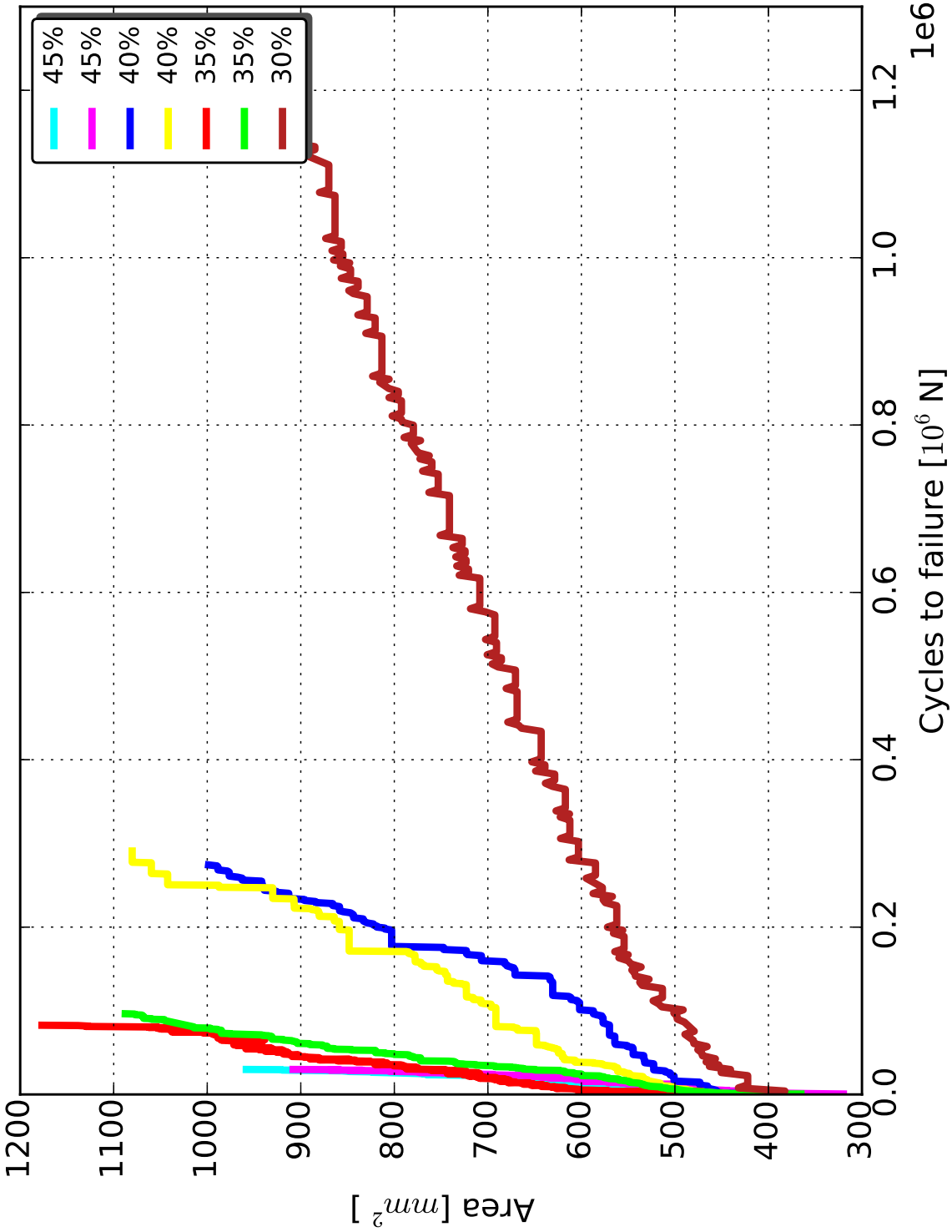

Figure 6.8: Delamination growth rate curves (Area vs cycles)

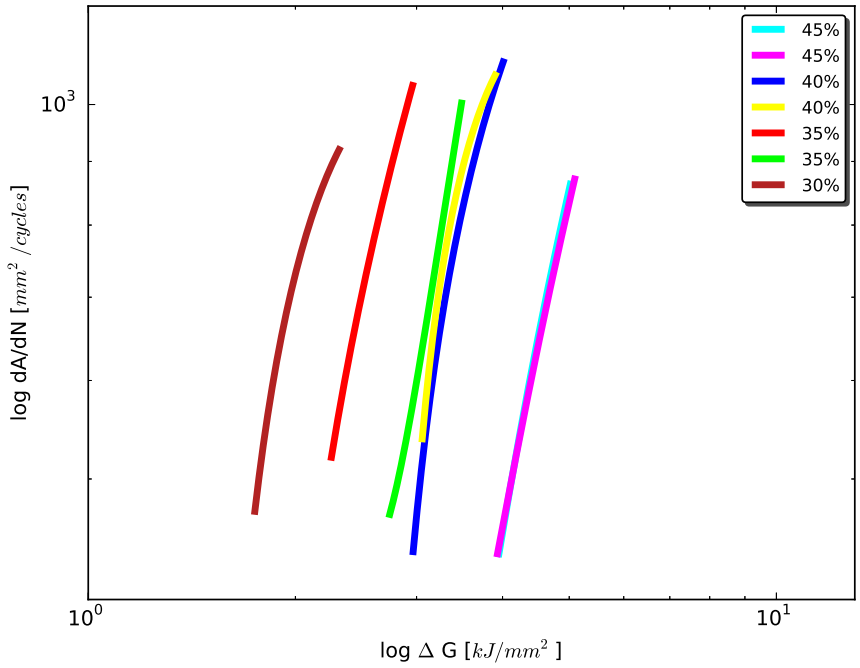

Figure 6.9: Fatigue propagation plots, ΔG vs $\frac{dA}{dN}$

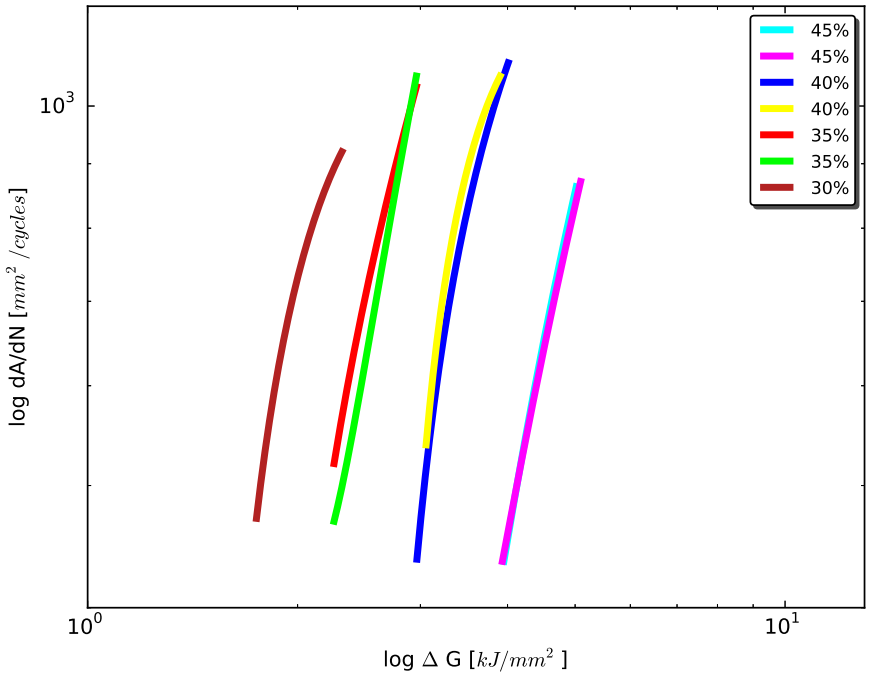

Figure 6.10: Corrected fatigue propagation plots, ΔG vs $\frac{dA}{dN}$

Furthermore, the fatigue propagation curves (ΔG vs $\frac{dA}{dN}$) were generated using a polynomial curve fitting approach. The fatigue propagation curves are as shown in Figure 6.9. As discussed earlier, the strain energy plots are corrected for the error. In this way, the fatigue propagation also changes as in Figure 6.10. The sample with high loads propagate to failure faster than the low load and all the samples displayed a similar trend. The trend in the propagation curves is similar to the propagation curves determined by conventional methods [63]. So, it is observed that the data measured from the IR camera gives promising results.

6.3 Comparison of IR data with visible light camera data

The results from the IR camera were compared with the area of delamination measured by a visible light camera. This was possible for glass fiber samples as they are partially transparent and thin; so the delamination is visible when viewed using a visible light camera. The area of delamination measured by the IR camera and visible light camera are tabulated in Table 6.1, where A_{IR} is the area determined by the IR camera and A_v is the area determined by the visible light camera.

Table 6.1: Comparison of area measured by the IR camera and visible light camera. The difference in percentage is calculated using $\frac{A_{IR}-A_v}{A_{IR}} * 100$

Cycles (10^3)	A_{IR} (mm^2)	A_v (mm^2)	**Difference** %
1	420	396	5.71
5	430	418	2.79
10	464	432	6.89
50	492	451	8.33
100	528	496	6.06
5000	657	597	9.13
10000	848	762	10.14

The sample used for this case is of similar configuration as mentioned earlier and the test was conducted at 35% of maximum static load. Once the test was completed, the IR camera data was processed as mentioned earlier. The delamination data from the visible light camera was analyzed using Photoshop software. The delamination data was manually evaluated at different intervals as seen in Table 6.1. The measured data from both cameras was plotted against the number of cycles. Both measurements show a similar trend but the area measured by the IR camera is always greater than the area measured with the visible light camera as seen in Figure 6.11.

The reason for difference in the delamination area is that the delamination in the visible light camera will appear once the event of delamination has occurred. However, in the case of the IR camera, the region where the delamination is occurring (under process) will have maximum temperature. As a result, IR images obtained with an IR camera reveal regions which are delaminating as completed delaminations. In case of visible light camera, a delamination can be detected only after actual separation of the material. Previous work by one of the authors [64] using optical coherence tomography (OCT) has shown that the regions at the edge of the crack have high stress and cannot be easily resolved with a visible light camera. However, the difference in calculation of the delamination area by the IR camera and the

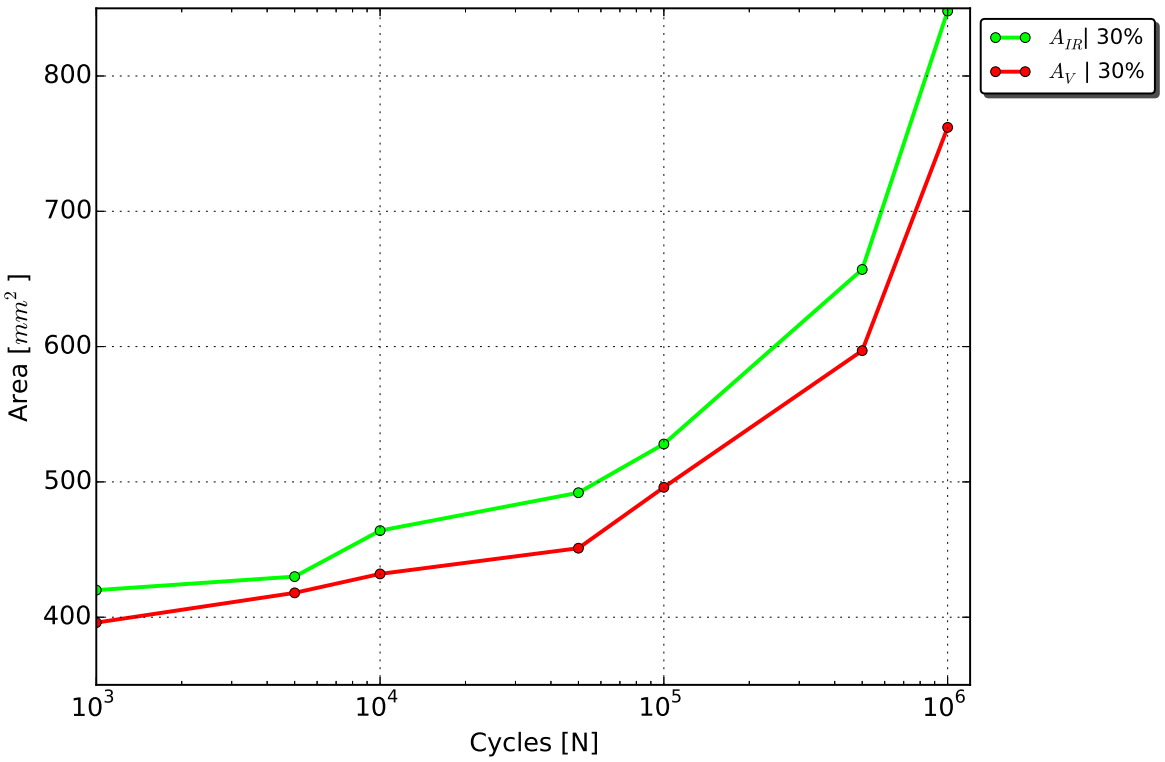

Figure 6.11: Comparison of measurement by the IR camera and visible light camera

visible light camera is less than 10% which is negligible considering the fact that the area from the visible light camera is calculated by manual method.

This chapter can be concluded by stating that the result obtained in this research was satisfactory and the fatigue propagation curves were plotted for different samples to evaluate their fatigue behaviour.

Chapter 7

Conclusion and recommendations

Chapter summary *In this current research, a new technique was developed to use the IRT to characterise the delamination under fatigue loading. In this chapter, firstly, the conclusions are presented as derived from the research results in Chapter 6. Finally, this report is concluded by giving some suggestions for future research. The recommendations made here are essentially based on the conclusions presented in this chapter.*

7.1 Conclusions from the research

The central investigation question of the research formulated in Chapter 2 was: ***"Can infrared thermography be a tool for quantitative analysis of damage in composites under dynamic loading?"***. Fundamentally, it was a feasibility study, where the intent was to check if it would be possible to extend the infrared technique to characterise the delamination growth in composites under fatigue loading. Prior to this research IRT was mostly limited to inspections and qualitative analysis of the defects.

To answer the preliminary question, sub-questions were raised. The sub-questions were:

1. *What kind of test samples and the experimental setup should be designed to answer the main question?*
2. *Which thermographic processing techniques to be used to evaluate damage growth?*

From the analysis of the results in Chapter 6, the primary question of using IRT to characterise defects under fatigue loading was successfully proved. Firstly, the delamination propagation curves obtained with the use of IR camera data showed a very good correlation with the damage growth curves and proved that this method can be effectively used for monitoring

delamination under fatigue loading. The samples with varying load levels had different crack growth speeds, the lower loads had lower speeds and the higher loads had higher speeds.

The design of the test sample and the experimental setup was very important to prove the method developed. As the results obtained looked promising with the fatigue properties and the correlation was established with the visible light camera, it can be assumed that the sample design and the experimental setup was more than satisfactory in this case.

The test machine and IR camera were not synchronised completely, there existed a mismatch of 2-5 seconds since the test machine was controlled by a dedicated software and the IR camera was controlled by a separate computer. If in case synchronisation was established, two types of benefits could have been acquired. Firstly, there could be no need to use a polynomial fit to obtain the fatigue propagation (Paris plots) curves. Secondly, most of the noise could be eliminated as the recording was synchronised with test machine making it easy for processing. Moreover, if the programme for processing was built into the system controlling the test, the output could have been obtained on the spot making it more like an in-situ online monitoring study. This would have helped in avoiding all the post-processing time making it simple and easy to study the fatigue properties of the given case on the go.

The image processing technique was a crucial part of this research as there were various processing techniques in the literature. Although, there existed various techniques, this research demanded to use a technique which could filter out data at a particular frequency. As mentioned in Chapter 6, it is practically challenging to capture a single image of the test while it was running. So, it was planned to record a video with few frames. Once the data is captured in the form of a video, it should be filtered at the test frequency to obtain the required output. With this requirement, the best processing technique was transforms. The widely used technique is Fourier transform however, a few researchers have started using wavelets transform recently. Wavelets transform play an important role if the research involves finding the depth of the defect which is not of prime importance in this research. Therefore, it was planned to go ahead with the Fourier transforms to check the feasibility of this research study. Further, it can be extended to different transforms and evaluate the difference to find the best suitable technique. The quality of the image when checked with the parameter called signal to noise ratio showed that the quality of the processed image had considerably increased thus confirming the technique to be competent.

After the images were processed, image segmentation was carried out using segmentation by threshold algorithm. Segmentation by the threshold is a simple but effective technique that provides promising results for images with fewer features.

Further, the results from the IR data was validated by comparing the results from the visible light camera used to capture the test along with IR camera. This comparison also gave very close results with a maximum variation of 10% in the delamination area. So to conclude the genuineness of data obtained from the IR camera has been validated at different stages. At first, with a signal to noise ratio data parameter of the images before and after processing and then, by comparing IR data with the visible light camera data.

From the aforementioned conclusions, it was proved that the research questions of this thesis project were answered, at least in a provisional manner, by the procedures demonstrated in the current project. This project provides a methodology that is promising and can be effectively used to study the delamination growth in composites under fatigue loading. Moreover, this method is also well defined and meaningfully validated with the help of a visible light camera.

Finally, the solution to the main research question is said to be answered in a provisional form because this research only acknowledged a specific material, test samples and testing circumstances. Without more extensible research like higher fatigue loads, other damage types or more complicated samples, the recommended methodology cannot be claimed as a universal and versatile method. Whatsoever, there seems to be no obvious reason to make the current methodology invalid in extending the investigation to the variants. As the results from this research was promising, it was presented at the European Conference on Composite Materials ECCM17, Munich, Germany [65].

7.2 Recommendations for future research

- The method explained in this research was to study the delamination growth with artificial delamination as an initial flaw in the sample which is a standard practice in damage tolerance analysis. The artificial delamination used in this research was stimulated by PTFE tape. There is no specific material to simulate delamination so in future, some more variation in material to simulate delamination can be explored and the effects on IR techniques can be studied.
- Delamination can be easily tracked using the current method, the 2D delamination shape can be visualised easily and the crack front can be clearly studied. Since this feasibility study was successful, this research can be further extended by comparing with the conventional method. With this comparison, the difference in the fatigue properties evaluated by different methods can be seen and the best one can be used to optimise the design.
- The current technique cannot be accepted universally as it is just a feasibility study. This method could be extended to various test samples such as a repair test sample and a bonded sample. This method can be an interesting choice for bonded composite samples as it helps to visualise the failure very clearly.
- Further, the research can be extended to different processing techniques like wavelet transforms, to evaluate the difference to find the best suitable technique.
- Finally, as this method provides quantitative test data, the test results obtained from this methodology can be a good input for a finite element model. Samples that cannot be studied using conventional techniques can be studied and implemented into the model to make them more reliable and expand their potential by using this method.

To conclude everything, the results from this method were promising as the delamination growth curve recorded using this method was in good agreement with a power law and visual inspection methods. The quantifiable measurements and the output of this method can be a good starting point to study delamination experimentally and computationally. This technique can be extended to different sample types that cannot be quantitatively analysed using the conventional testing methods.

References

[1] M. Michael and R. Hallett. Damage initiation in polymer matrix composites under high-cycle fatigue loading - a question of definition or a material property? *International Journal of Fatigue*, 87:59–62, 2009.

[2] United States Government Accountability Office. Status of FAA's actions to oversee the safety of composite airplanes. *Highlights of GAO-11-849, a report to congressional requesters*, 2011.

[3] L. James. On the cutting edge : Next generation materials in turbine blade construction. http://www.renewableenergyworld.com/articles/print/special-supplement-wind-technology/volume-2/issue-2/wind-power/on-the-cutting-edge-next-generation-materials-in-turbine-blade-construction.html, 2015.

[4] M. G. Richard. Impressive beast, world's longest wind turbine rotor blade measures 246 feet. http://www.treehugger.com/renewable-energy/worlds-longest-wind-turbine-rotor-blade-measures-246-feet.html, 2012.

[5] M. Shokrieh and R. Rafiee. Simulation of fatigue failure in a full composite wind turbine blade. *Composite structures*, 74:332–342, 2006.

[6] J. Lambert, A. R. Chambers, I. Sinclair, and S. M. Spearing. Damage characterisation and the role of void in the fatigue of wind turbine blade materials. *Conference paper : Composites science and technology*, 2012.

[7] R. Kim and S. Soni. Experimental and analytical studies on the onset of delamination in laminated composites. *Journal of Composite materials*, 18:70–80, 1984.

[8] C. Lin and P. Kao. Delamination growth and its effect on crack propagation in carbon fiber reinforced aluminum laminates under fatigue loading. *Acta Materialia*, 44(3):1181–1180, 1996.

[9] M. Hojo, S. Matsuda, M. Tanaka, S. Ochiai, and A. Murakami. Mode 1 delamination fatigue properties of interlayer-toughened cf-epoxy laminates. *Composites Science and Technology*, 66:665–675, 2006.

[10] J. Marin, A. Barroso, F. Paris, and J. Canas. Study of fatigue damage in wind turbine blades. *Engineering Failure Analysis*, 16:656–668, 2009.

[11] B. Groenenboom. Acoustic emission monitoring of fatigue damage progression in composite ship structures. *Master thesis, Delft University of Technology*, 2016.

[12] K. Peycheva. Nondestructive testing of metals and composite materials using ultrasound thermography: Comparison with pulse-echo ultrasonics. *Master thesis at University Laval Quebec*, 2012.

[13] L. Toubal, M. Karama, and B. Lorrain. Damage evolution and infrared thermography in woven composite laminates under fatigue loading. *International Journal of Fatigue*, 28(12):1867–1872, 2006.

[14] H. Schmutzlera, M. Aldera, N. Kosmanna, H. Witticha, and K. Schulte. Degradation monitoring of impact damaged carbon fibre reinforced polymers under fatigue loading with pulse phase thermography. *Composites Part B: Engineering*, 59:221–229, 2014.

[15] K. Kurashiki, Q. Ni, T. Maesaka, and M. Iwamoto. A study on evaluation of fatigue damage of gfrp by infrared thermography. *Japan Society of Mechanical Engineers*, 66(645):960–965, 2000.

[16] C. Colombo and L. Vergani. Influence of delamination on fatigue properties of a fibreglass composite. *Composite Structures*, 107:325–333, 2014.

[17] J. Narayana Swamy. Infrared thermography technique to monitor the behaviour of composites with defect under dynamic loading at coupon level. *Literature Survey, Delft University of Technology*, 2016.

[18] S. Long, X. Yao, and X. Zhang. Delamination prediction in composite laminates under low velocity impact. *Composite Structures*, 132:290–298, 2015.

[19] C. Nageswaran, C. R. Bird, and R. Takahashi. Phased array scanning of artificial and impact damage in carbon fibre reinforced plastic. *The 44th Annual British Conference on NDT*, 48(3), 2005.

[20] J. Pascoe, R. Alderliesten, and R. Benedictus. Method for the prediction of fatigue delamination growth in composites and adhesive bonds - a critical review. *Engineering fracture mechanics*, 112-113:72–96, 2013.

[21] J. Renton and J. Vinson. On the behavior of bonded joint in composite structures. *Engineering fracture mechanics*, 7:41–60, 1975.

[22] G. Stefanos. Utilising fracture mechanics principles for predicting the mixed-mode delamination onset and growth in tapered composite laminates. *Composite Structures*, 102:294–305, 2013.

[23] I. Ashcroft and S. Shaw. Mode 1 fracture of epoxy bonded composite joints 2. fatigue loading. *International Journal of Adhesion and Adhesives*, 22:151–167, 2002.

[24] K. Reifsnider, J. Lesko, and S. Case. Damage mechanics and nde of composite laminates. *IUTAM-Symposium Mechanical Composite Materials*, pages 399–420, 1983.

[25] N. Gathercole, H. Reiter, T. Adam, and B. Harris. Life prediction for fatigue of t800/5245 carbon-fibre composite: I. constant-amplitude loading. *International Journal of Fatigue*, 16(8):523–532, 1994.

[26] K. L. Reifsnider and R. S. Williams. Determination of fatigue-related heat emission in composite materials. *Experimental Mechanics*, 14(12):479–485, 1990.

[27] G. Pitarresi1, L. D. Acquisto, and A M Siddiolo. Thermoelastic stress analysis by means of an infrared scanner and a two-dimensional fast fourier transformbased lock-in technique. *Strain Analysis*, 43:324–329, 2008.

[28] F. Lahuerta, R. P. L. Nijssen, F. P. van der Meer, and L. J. Sluys. Experimental-computational study towards heat generation in thick laminates under fatigue loading. *International Journal of Fatigue*, 80:121–127, 2015.

[29] C. Colombo and L. Vergani. Influence of delamination on fatigue properties of a fibreglass composite. *Composite Structures*, 107:325–333, 2014.

[30] F. Lahuerta, R. P. L. Nijssen, F. P. van der Meer, and L. J. Sluys. Infrared inspection of thick laminates during fatigue tests. *7th International conference on composite testing and model identification*, 2015.

[31] R. C. Tighe, J. M. Dulieu-Barton, and S. Quinn. Identification of kissing defects in adhesive bonds using infrared thermography. *International Journal of Adhesion Adhesives*, 64:168–178, 2016.

[32] R. Hidalgo-Gato, J. R. Andres, J. M. Lopez-Higuera, and F. J. Madruga. Quantification by signal to noise ratio of active infrared thermography data processing techniques. *Optics and Photonics Journal*, 3:20–26, 2013.

[33] SAERTEX. *Data sheet, Article No : S15EU910-00950-00600-100000.*

[34] Hexion. *Technical data sheet EPIKOTE Resin MGS RIMR 135 and EPIKURE Curing Agent MGS RIMH 134-RIMH 137.*

[35] F. Aymerich. Composite materials for wind turbine blades: issues and challenges. *SYSWIND Summer school*, University of Patras, 2012.

[36] M. Tarin and R. Rotolante. *FLIR Technical Series,NDT in Composite Materials with Flash, Transient, and Lockin Thermography*, 2011.

[37] NEN-EN-ISO 527-5. *Plastics - Determination of tensile properties - Part 5: Test conditions for unidirectional fibre-reinforced plastic composites*, 2009.

[38] C. Rans, J. Atkinson, and C. Li. On the onset of the asymptotic stable fracture region in the mode ii fatigue delamination growth behaviour of composites. *Journal of Composite Materials*, 0:1–13, 2014,.

[39] ASTM D2584 11. *Standard Test Method for Ignition Loss of Cured Reinforced Resins*, 2011.

[40] P. Bortolotti. *Carbon Glass Hybrid Materials for Wind Turbine Rotor Blades.*

[41] F. Lahuerta and R.P.L. Nijssen. Infrared inspection of thick laminates during fatigue tests. *7th International conference on composite testing and model identification*, 2015.

[42] C. Lina, C. Kuod, C. Laie, M. Tsaib, Y. Changa, and H. Cheng. A novel approach to fast noise reduction of infrared image. *Infrared Physics & Technology*, 54:1–9, 2011.

[43] K. Gupta, M. Rizwan, and J. Niranjan. A novel approach to fast image filtering algorithm of infrared images based on intro sort algorithm. *IJCSI International Journal of Computer Science Issues*, 6(1):235–241, 2011.

[44] S. Budzan and R. Wyzgolik. Remarks on noise removal in infrared images. *Measurement Automation Monitoring*, 61(06):187–190, 2015.

[45] C. Ibarra-Castanedo, D. Gonzalez, M. Klein, M. Pilla, S. Vallerand, and X. Maldague. Infrared image processing and data analysis. *Advanced Infrared Technology and Application*, 46(1-2):75–83, 2004.

[46] M. Alhussein and S. Haider. Simulation and analysis of uncooled microbolometer for serial readout architecture. *Journal of Sensors*, 16:13, 2016.

[47] C. Castanedo, A. Bendada, and X. Maldague. Thermographic image processing for ndt. *IV Conferencia Panamericana de end Buenos Aires*, 2007.

[48] X. P Maldague. Theory and practice of infrared technology for nondestructive testing. *John Wiley Sons*, 2001.

[49] R. Martin, A. Gyekenyesi, and S. Shepard. Interpreting the results of pulsed thermography data. *Materials Evaluation*, 61(5):611–616, 2003.

[50] R. Hidalgo-Gato, J. R. Andres, J. M. Lopez-Higuera, and F. J. Madruga. Quantification by signal to noise ratio of active infrared thermography data processing techniques. *Optics and Photonics Journal*, 3:20–26, 2013.

[51] S. Marinetti, E. Grinzato, P.G. Bison, E. Bozzi, M. Chimenti, G. Pieri, and O. Salvetti. Statistical analysis of ir thermographic sequences by pca. *Infrared Physics Technology*, 46:85–91, 2004.

[52] X. Maldague and S. Marinetti. Pulse phase infrared thermography. *Journal of Applied physics*, 79:47–70, 1995.

[53] R. Tighea, G. Howella, J. Tyler, S. Lormorc, and J. Dulieu-Bartona. Stress based nondestructive evaluation using thermographic approaches: From laboratory trials to on-site assessment. *NDT and E International*, 84:76–88, 2015.

[54] P. Shin, S. Webb, and K. Peters. Pulsed phase thermography imaging of fatigue-loaded composite adhesively bonded joints. *NDT and E International*, 79:7–16, 2014.

[55] A. Poudel, K. Mitchel, T. Chu, S. Neidigk, and C. Jacques. Non-destructive evaluation of composite repairs by using infrared thermography. *Journal of Composite Materials*, 50(3):351–363, 2016.

[56] S. Pawar and V. Vavilov. Applying the heat conduction-based 3d normalization and thermal tomography to pulsed infrared thermography for defect characterization in composite materials. *International Journal of Heat and Mass Transfer*, 94:56–65, 2016.

[57] M. Jogendra, R. Vijay, and R. Kumar. Review on image segmentation technique. *International Journal of Scientific Research Engineering Technology*, 3(6), 2016.

[58] S. Saini and K. Arora. A study analysis on the different image segmentation techniques. *International Journal of Information Computation Technology*, 4(1445-1452), 2014.

[59] V. Guruswamy, S. Kannan, and G. Nalini. Review on image segmentation techniques. *Conference: RTRICS, Podi*, 2014.

[60] H.P. Narkhede. Review on image segmentation techniques. *International Journal of Science and Modern Engineering*, 1(8):16–21, 2013.

[61] D. Kaur and Y. Kaur. Various image segmentation techniques, a review. *International Journal of Computer Science and Mobile Computing*, 3(5):809–814, 2014.

[62] F. Lahuerta, R. P. L. Nijssen, F. P. Van Der Meer, and L. J. Sluys. Experimental & computational study towards heat generation in thick laminates under fatigue loading. *Int. J. Fatigue*, 80:121–127, 2015.

[63] F. Lahuerta, T. Westphal, R. P. L. Nijssen, F. P. Van Der Meer, and L. J. Sluys. Measuring the delamination length in static and fatigue mode i tests using video image processing. *Compos. Part B*, 63:1–7, 2014.

[64] P. Liu, R. M. Groves, and R. Benedictus. Ndt & e international 3d monitoring of delamination growth in a wind turbine blade composite using optical coherence tomography. *NDT&E Int.*, 64:52–58, 2014.

[65] J.K.Narayana Swamy, F.Lahuerta, A.G.Anisimov, R.P.L.Nijssen, and R.M.Groves. Evaluating delamination growth in composites under dynamic loading using infrared thermography. *ECCM17 - 17TH European conference on composite materials*, 2016.